UNIVERSIDADE FEDERAL DO PAMPA
CAMPUS ALEGRETE
PROGRAMA DE PÓS GRADUAÇÃO EM ENGENHARIA

NUMERICAL SOLUTION FOR THE DROPLET COMBUSTION

DISSERTAÇÃO DE PÓS GRADUAÇÃO

Mariovane Sabino Donini

Alegrete

2017

MARIOVANE SABINO DONINI

NUMERICAL SOLUTION FOR THE DROPLET COMBUSTION

Alegrete

2017

MARIOVANE SABINO DONINI

NUMERICAL SOLUTION FOR THE DROPLET COMBUSTION

Dissertação de Pós Graduação apresentada ao Programa de Pós Graduação Stricto sensu em Engenharia da Universidade Federal do Pampa (UNIPAMPA, RS), como requisito parcial para obtenção do grau de Mestre em Engenharia.

Área de concentração: Fenômenos de Transporte

Banca examinadora:

_____

Prof. Dr. Cesar Flaubiano da Cruz Cristaldo
Orientador
(UNIPAMPA)

_____
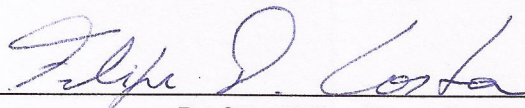
Prof.Dr. Felipe Denardin Costa
(UNIPAMPA)

_____
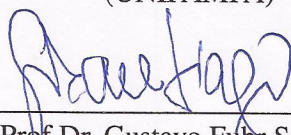
Prof.Dr. Gustavo Fuhr Santiago
(UNIPAMPA)

_____
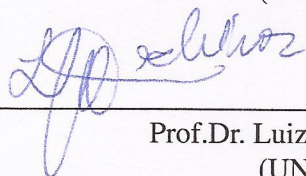
Prof.Dr. Luiz Eduardo Medeiros
(UNIPAMPA)

ACKNOWLEDGEMENTS

We are star stuff which has taken its destiny into its own hands. The loom of time and space works the most astonishing transformations of matter.

Carl Sagan

ABSTRACT

In the present work, vaporization and combustion of an isolated fuel droplet at different ambient temperatures are examined numerically in order to analyze the effect of buoyancy force on the flame. Generally, fuel droplets in combustion devices are so small that the influence of buoyancy force on vaporization and combustion of droplets is negligible. On the other hand, fuel droplets in experimental devices are affected by the buoyancy force due to their diameters being around or more than 1 mm. To reduce the buoyancy effects, expensive experimental studies are performed in microgravity ambient (drop-tower or out of space). In normal-gravity conditions, the buoyancy force is induced by temperature gradient on ambient atmosphere. The buoyancy is positive in regions of hot gases and negative in regions of cold gases compared with the ambient atmosphere gas. Hot gases move upward and cold gases downward. Playing with the positive buoyancy force of hot gases around the flame and with the negative (cold) buoyancy force of cold gases around the droplet via ambient atmosphere temperature, it is possible to modify the flame shape. In the numerical simulations, incompressible Navier–Stokes equations along with mixture fraction and excess enthalpy conservation equations are solved using a finite volume technique with a uniform structured grid. An artificial compressibility method was applied to reach steady state solutions. The numerical predictions have been compared with analytical results for a zero gravity condition, showing good agreement. For normal gravity condition the numerical results showed that when the ambient temperature increases, the velocity gradient and buoyancy source term decreases. Despite that, the flame increased in all directions. The results have also shown that increasing the ambient temperature, decreases the temperature gradient in the flame, which ends up affecting the flame position.

Keywords: Droplet Combustion, Microgravity, Natural Convection.

LIST OF FIGURES

LIST OF TABLES

LIST OF SYMBOLS

a   droplet radius

c_p specific heat

d_0 initial droplet diameter

Da Damköhler number

Fr Froude Number

F convective mass flux per unit of area

Gr Grashof Number

g local acceleration due to gravity (m/s^2)

H excess enthalpy

K evaporation constant

k thermal conductivity (W/mK)

Le Lewis Number

$\dot{m}$ vaporization rate

P pressure (N/m^2)

Pr Prandtl Number

Q combustion heat

r radial coordinate (m)

s_i reactant mass (fuel or oxidant)

t_c heating time

T temperature (K)

Y_F fuel mass fraction (kg/kg)

Y_O oxidant mass fraction (kg/kg)

v   velocity (m/s)

$\dot{w}$ net rate of work done

Z mixture fraction

Greek letters

α thermal diffusivity (m^2/s)

ν kinematic viscosity (m^2/s)

ν_O mass of oxidant consumed

ρ density (kg/m^3)

Subscripts and Superscripts

$*$ dimensional property

∞ ambient atmosphere condition

b boiling point

e east

F fuel

i fuel or oxidant

l liquid phase

n north

O oxidant

s south

w west

CONTENTS

1 INTRODUCTION

Droplet combustion is important for variety of different applications like, diesel engines, gas turbines, and rocket motors. In those applications the initial phase is the spraying of liquid fuel (cloud of droplets) into an oxidizing atmosphere followed by its vaporization and combustion, called spray combustion. Spray combustion enables energy to be release through atomization of the liquid fuel and the subsequent vaporization and combustion of the resulting droplet spray. The study of this process is extremely important to determine the efficient usage of energy, and to better understand the mechanisms of pollutant formation (ANNAMALAI; PURI, 2006). Droplet combustion is a vastly studied topic. However, the accurate prediction of all the physical and chemical phenomena over all realistic ranges of parameters has not yet been achieved due to its complexity (HEYWOOD, 1988).

Many efforts to understand such phenomena have focused upon studying isolated droplets. Information gained from these studies is often not directly transferable to spray situations. However, isolated-droplet studies are useful in that they allow certain phenomena (e.g., extinction) to be studied under well-controlled and simplified conditions. When theory and experiment agree for simplified situations, predictions for more complex cases (where accurate experimental data may not exist) may be made with more confidence (PURI, 1993). Thus, various previous researches have investigated, both experimentally and by numerical simulation, the vaporization of a single droplet and the droplet interaction under different conditions (WILLIAMS, 1973; LAW, 1982; FAETH, 1983; ABRAMZON; SIRIGNANO, 1989).

Isolated droplet combustion experiments are of practical interest because their behavior provide an understanding of the fundamental mechanisms which are present in a spray (SPALDING, 1953). In engineering applications, the small droplets ($1 - 100\mu m$ diameter) of the spray are not greatly affected by buoyancy. Thus the droplet vaporization present a spherically symmetric configuration. On the other hand, experiments in laboratory are performed with large droplets, (diameter of the order of millimeter). The effects of buoyancy in these experiments (for large droplets) have seriously compromised our capabilities to carry out experiments needed to advance our understanding of flame phenomena on droplet combustion. To avoid buoyancy effects, the droplet combustion is submitted to a microgravity environment to achieve a spherically symmetrical combustion.

1.1 Objectives

Considering the difficult and the cost of large droplet combustion experiments in microgravity, numerical experiments of the combustion of an isolated droplet are performed to analyze the effect of buoyancy force on the flame. Recalling that, the increasing ambient temperature results in the decrease of the gradient temperature of the gas-phase, which results in the decrease of buoyancy force.

This effect can be investigated directly in the buoyancy source term of the non-dimensional momentum conservation equations, where appears the Froude Number associated with buoyancy-driven flow. Therefore, it is possible to investigate the parameters of interest directly on the buoyancy source term, like gravity, droplet diameter and the variation of temperature.

2   LITERATURE REVIEW

Since liquid fuel possesses high energy content per unit mass and are relatively safe to store and transport, they are of great interest in many practical applications like electric power production, industrial burners, space propulsion or diesel engines. The performance of these devices depend greatly on the injection processes including fuel atomization, evaporation, and mixture formation preceding combustion itself (WILLIAMS, 1990; TURNS, 2000; KUO, 2005). The atomization is responsible for increasing the contact surface between the fuel and hot combustion gases, improving heat transfer from the gases to the liquid fuel. Thus, the liquid fuel is atomized as a cloud of small droplets in the combustion chamber, which then vaporize and oxidize to release heat. The combustion performance and emission control are mainly influenced by the atomization of the fuel, the dispersion and evaporation of the fuel droplets and the mixing of fuel and air in the combustion chamber. In addition, the transport processes involved in vaporization of sprays are complex and involve advection, conduction, convection and mass transfer (SIRIGNANO, 1999).

In many spray combustion devices, the spray is formed by a high-pressure injection of liquid fuel trough a small nozzle hole into a gaseous environment. The liquid enters the combustion chamber at very high velocity in the form of a liquid jet, tends to become unstable and disintegrates into fragments, and then further dissolves into smaller isolated droplets, as illustrated in Fig. 1. Understanding isolated droplet burning is an essential prerequisite to deal with more complex flames. Therefore, droplet combustion models have been proposed under different scenarios.

Figure 1 – Schematic illustration of spray structure.
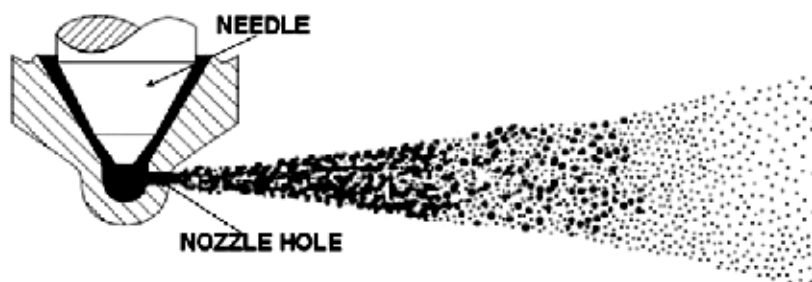
Source: Adapted from Vujanović (2010).

2.1 Classical Droplet Combustion Analysis (Microgravity)

The first model of droplet combustion was formulated by Spalding (1953) and Godsave (1953). They derived the classical d^2-law model that is capable of describing the vaporization process of a droplet. This model demonstrates that during the vaporization process, the droplet surface area, represented by the droplet squared diameter, decreases linearly with its lifetime:

$$d^2 - d_0{}^2 = Kt \tag{2.1}$$

Where d_0 is the initial droplet diameter and K is defined as a constant characterizing the rate of decrease in the size of the droplet which is called the vaporization constant. The value of the K is determined from the slope of the plot of droplet diameter squared versus time. Once the droplet reaches its boiling point, little heat is conducted into the liquid interior and the vaporization rate reaches its quasi-steady value.

A quasi-steady assumption is utilized in Spalding's analysis. This assumption is based on the relatively slow regression rate of the fuel droplet as compared to gas phase transport processes. Using this assumption, one can imagine that the droplet vaporizes so slowly that the droplet can be replaced by a porous sphere of a fixed diameter; the surface of this sphere is wetted by the liquid fuel, and the mass vaporization rate of fuel from its surface into the warm surrounding is equal to the feeding rate of the liquid fuel from a small feeding tube to the porous sphere.

Isoda e Kumagai (1958) performed the first spherically symmetric droplet combustion experiments trough free fall in a drop tower facility. Based on their studies, they proposed the combustion model shown schematically in Fig. 2. The temperature and the oxygen concentration are assumed to remain unchanged outside of the hot air zone; distributions of temperature and oxygen concentration in the hot air zone are approximated to those of heat conduction and diffusion in steady state in which the temperature and the oxygen concentration at the flame boundary are fixed to T_f and 0, and at the outside boundary of the hot air zone to T_∞ and Y_∞. The position of the hot air zone boundary could be located very distant from the droplet surface. However, for practical purposes, this boundary can be quite close to the fuel surface, as long as the temperature is asymptotically close to the ambient temperature, T_∞; the fuel and the oxygen in the air are assumed to react in stoichiometric proportion. The liquid droplet is surrounded by fuel vapor that diffuses outward from the droplet surface to the flame interface while oxidizer diffuses radially inward from the ambiance towards the flame interface. Fuel and oxidizer react fully, consuming one another in the flame zone as they diffuse towards each other resulting in the flame being represented as an infinitesimally thin sheet.

Figure 2 – Schematic diagram of a droplet combustion process.
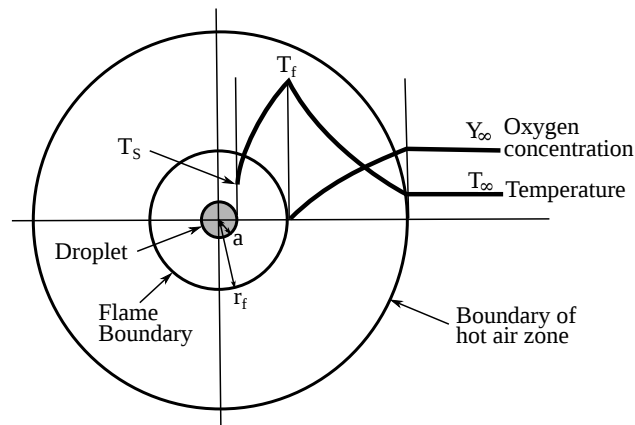
Source: Adapted from Isoda e Kumagai (1958).

According to Ulzama e Specht (2007) and Suh (2015), this model deals with the main following assumptions:

- Steady-state burning and spherical symmetry: Steady state combustion eliminates the time-dependent terms from the conservation equations, and diffusion only occur in the radial direction due to spherical symmetry.

- Quasi-steady assumption of gas-phase: Rate of changes in the gas-phase parameters are much faster than the corresponding liquid-phase parameters (Surface regression rate is much smaller than the flow velocities).

- Constant gas-phase transport properties: All thermophysical properties remain constant with temperature, and combustion products do not affect the process.

- Stoichiometric oxidant/fuel ratio at flame interface: Fuel and oxidizer fluxes from the droplet surface and infinity, respectively, to the flame zone must be in stoichiometric proportions.

- Infinitely fast gas-phase chemical reaction: Reaction is infinitely fast with respect to diffusion. This results in an infinitesimally thin flame interface where fuel and oxidizer are entirely consumed with no reactant leakage through the flame.

- Heat loss due to radiation is negligible.

- Unity Lewis number for all gas-phase: The diffusivities of both reactants are equal to the thermal diffusivity. This allows the combination of energy and species mass conservation equations to eliminate rate-dependent source terms.

- Constant and uniform droplet temperature: Droplet is assumed to be near its boiling temperature. This assumption neglects heat-up of the droplet.

Figure 3 shows a photograph of nearly spherical flame configuration obtained by burning a fuel droplet suspended at the end of a quartz fiber in a quiescent environment of reduced buoyancy.

Figure 3 – Photographic image of an almost spherically symmetric droplet combustion configuration, obtained for a suspended drople in reduced pressure and hence buoyancy.
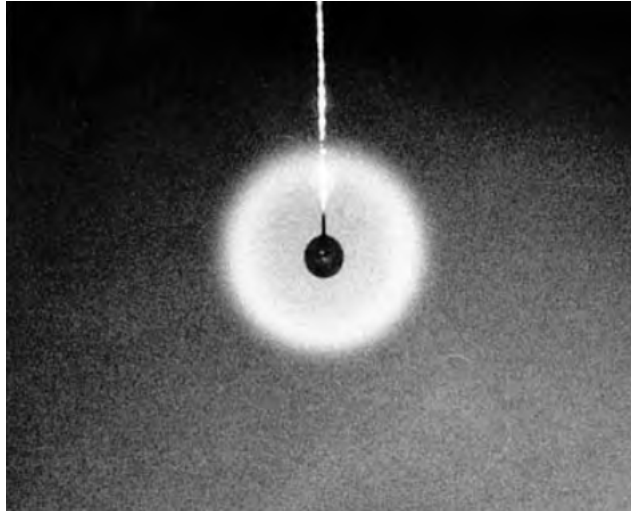
Source: Law (2006).

An advantage of the spherical symmetry found on classical analysis of droplet combustion is that only one spatial dimension enters the description of the combustion process, so that one-dimensional time-dependent conservation equations apply, facilitating both computational and theoretical descriptions of the combustion (DIETRICH et al., 2014).

2.2 Droplet Combustion in a Forced Convection Environment

Often, in many practical applications there exist an relative motion between the droplet and surrounding gas. Under the hypothesis that droplets maintain spherical shapes, there are many studies available on droplets vaporization under forced convection (PRAKASH; SIRIGNANO, 1980; RENKSIZBULUT; YUEN, 1983; MEGARIDIS; SIRIGNANO, 1991; CHIANG; RAJU; SIRIGNANO, 1992).

When the relative velocity is small, the flow configuration is slightly distorted from spherical symmetry. In this case, the gas-phase should be qualitatively similar to the spherically symmetric situation. The mathematical analysis, however, is significantly more complicated because of the additional dependence on the nonradial coordinates. Since gas-phase transport rates enhances with this additional nonradial convection, the burning rate is also expected to be increased. In some experiments the presence of natural convection increases the airflow velocity near the droplet, especially at elevated pressure, so even though forced convection exists,

microgravity environments are essential for purely forced convection experiments on droplet combustion (MITSUYA et al., 2005).

With very intense convection, the flame surrounding the droplet can be "blown off." The droplet now undergoes pure vaporization with a significantly reduced gasification rate. The fuel vapor generated at the droplet surface is then swept leeward where it mixes with the oxidizing gas to a certain extent. Combustion is sometimes possible in the wake region of the droplet, resulting in a wake flame. The phenomenon of blow-off the enveloping nonpremixed flame is essentially an extinction event, caused by extinction of the flame in the front stagnation region.

As discussed above, when a droplet burns in a convective environment it can supports different flame configurations, namely, envelope flame and wake flame.

- Envelope flame: at a moderate relative gas/droplet velocity, Fig. (4a), the flame completely envelopes the fuel sphere.

- Wake flame: under high relative gas/droplet velocity, the flame segment in the forward portion of the sphere appears to be "extinguished", and that combustion takes place only in the wake region, Fig. (4b).

Figure 4 – Schematic illustration of various flame configurations (a) sphere with envelope flame, Re = 92; (b) sphere with wake flame, Re = 152.

(a)   (b)
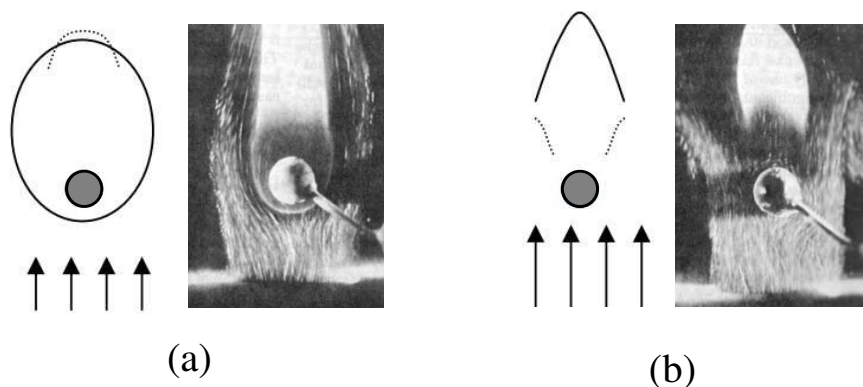
Source: Adapted from Gollahalli e Brzustowski (1973).

2.3 Normal Gravity Droplet Combustion

Most theoretical investigations neglect the influence of gravity due the simplifications afforded by spherical symmetry. The influence of gravity prevents the observation of the phenomena at a fundamental level found in most practical engineering applications. Thus it is necessary to know the mechanisms responsible for the natural convection in normal gravity.

The basic droplet combustion model, depicted in Fig. 5a, describes the combustion of the liquid fuel at the droplet surface and its subsequent outward transport to meet inwardly-diffusing oxidizing gas in a spherically thin flame region. On other hand, the flame shown schematically on Fig. 5b is severely elongated by the presence of buoyant flow. In this case, the flame shape is defined by three different dimensions, namely, standoff radius, s_f, flame height, h_f, and flame width, w_f, as illustrated in Fig. 5b. Fig. 6 shows the instantaneous images of flame configurations for diesel droplets burned for experiments without (Fig. 6a) and with buoyancy (Fig. 6b). The combustion in normal gravity (Fig. 6b) shows strong convection, as indicated by the crown extending upward from the droplet, like the schematic proposed by Law e Faeth (1994).

Figure 5 – Schematic of droplet envelop flames at (a) microgravity, and (b) normal gravity.

(a)   (b)
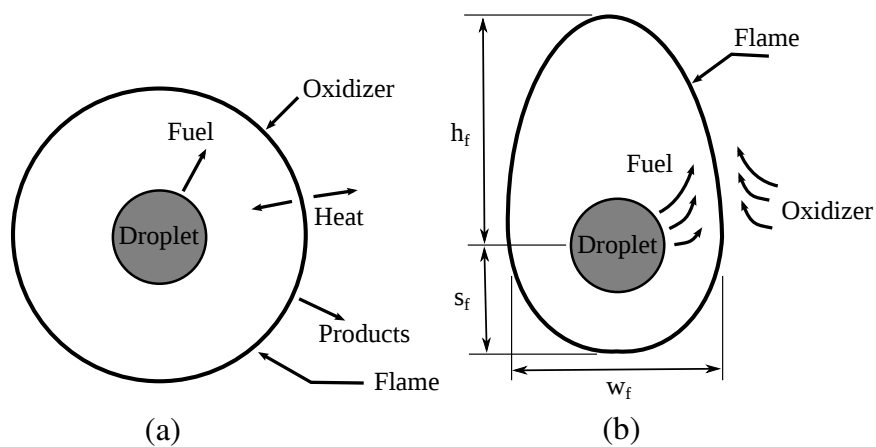
Source:Law e Faeth (1994).

Figure 6 – Instantaneous visualization of a burning diesel droplet showing flame configuration for: (a) $D_0 = 445$ μm reduced gravity, and (b) $D_0 = 445$ μm at normal gravity.

(a)   (b)
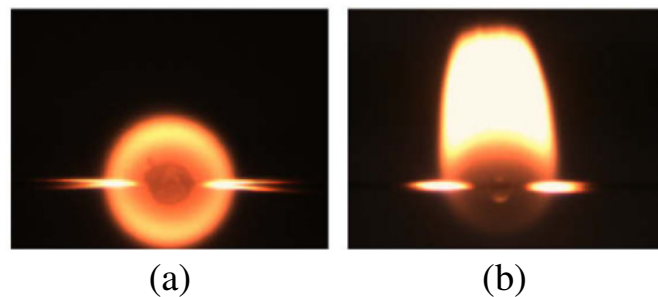
Source: Adapted from Pan et al. (2009).

To minimize these effects of natural convection, one must reduce buoyant transport relative to diffusive transport of the fuel vapor towards the flame. The Grashof number represents the ratio of these transport mechanisms:

$$Gr = \frac{(\Delta\rho/\rho)gd_s^{3}}{v^2} \tag{2.2}$$

Where $\Delta\rho$ is the characteristic density change, ρ is the mean density, g is the local acceleration due to gravity, d_s is the droplet diameter and ν is the kinematic viscosity.

According to Yozgatligil et al. (2004), there are three parameters that can be adjusted to reduce the system Grashof number: the initial diameter, ambient pressure and effective gravity. Reducing initial droplet diameter limits the ability to accurately resolve transient processes such as ignition, soot formation and flame extinction. When the droplet is very small, the surrounding gases can entrain easily and the relative velocity between the droplet and nearby gases becomes small; then, the diffusion flame surrounding the droplet becomes nearly spherical (KUO, 2005). Although reducing the pressure decreases the Grashof number through an increase in diffusivity, the lowest pressure at which a droplet can be ignited does not provide spherically symmetric flames. The Grashof number also can be reduced by performing experiments in microgravity facilities discussed in the next section. Another alternative to change the ratio between buoyant transport and diffusive transport is to vary the ratio of density $(\Delta\rho/\rho)$, by adjusting the environment temperature relative to the droplet surface temperature.

2.4 Studies in Droplet Combustion

2.4.1 Experimental Studies

There are many experiments to evaluate microgravity combustion, like studies utilizing drop-tower facilities and/or parabolic flights and extended duration testing on orbiting facilities (EIGENBROD, 1999). These experiments provide vital information concerning how fires behave in microgravity and how fire safety on spacecraft can be enhanced (KING; ROSS, 1998).

Dietrich et al. (1996) performed droplet combustion experiments in space-based platforms aboard the space shuttle Columbia with droplets initial diameters of 3.5 mm and 5.2 mm. Individual droplets were tethered by a silicon carbide fiber and burned under microgravity conditions in air at 1 bar with an ambient temperature of 300 K. The results demonstrated that the combustion of fuel droplets as large as *5mm* in diameter happens in ways expected by the theory. Forced convective flow around methanol droplets was found to increase the burning rate and to produce a ratio of downstream to upstream flame radius that remained constant as the droplet size decreased.

Manzello et al. (2000) performed experiments to analyze the burning and sooting behavior of large n-heptane droplets in microgravity. The experiments were performed at the Japan Microgravity Center (JAMIC) drop shaft. The JAMIC facility is the longest drop shaft in the world and provides 10 seconds of gravity levels less than 10^{-5}g. The droplets were tethered using silicon carbide fibers, used to prevent drifting of the droplet out of the field of view during the observation period.The results demonstrated that sooting tendency is reduced for large droplets

and the lower soot volume fractions were accompanied by higher burning rates and lower flame emissions.

Choi e Kyeong-Okk (1996) analyzed n-heptane droplets burning under microgravity conditions for droplet diameters ranging from 0.8 mm to 1.8 mm and Yozgatligil et al. (2007) investigated the large ethanol droplets (diameters ranging from 1 to 3 mm) under microgravity conditions, both in the 2.2s droptower at the NASA Glenn Research Center. The results suggested that larger droplets would be required to better describe the effects of sooting and radiation in their experiments. However, the duration of the microgravity observation time available in the 2.2 s droptower was insufficient to extend the investigation for larger droplets. Larger droplets require longer preparation time for droplet formation, deployment, ignition, and the oscillation decay period caused by these procedures.

Chauveau, Birouk e Gökalp (2011) examined experimentally n-decane droplet vaporization. Two sets of experiments were performed, one in normal gravity and another in microgravity conditions. The latter were done using the parabolic flights aboard the A300 Airfcraft of CNES (The French Space Agency). The environment temperature was varied in range up to $967K$. The droplet was suspended onto the cross point of two micro-fibers. The results show that, for ambient temperatures exceeding approximately $950K$, the d^2-law holds throughout the entire droplet lifetime, and the mass transfer rate is identical in both microgravity and normal gravity environments.

2.4.2   Numerical Studies

Numerical studies on fuel droplets under normal and microgravity ambients are also available in the literature. Dwyer e Sanders (1988) have presented numerical solutions of steady flowfields around burning fuel droplets at constant Reynolds number under buoyancy induced flow conditions. The study has been restricted to gas-phase combustion processes, therefore droplet internal circulation has been ignored and the droplet was assumed to be at a constant temperature near the boiling point. The numerical results were compared with experimental measurements in the literature of envelope and wake flames on porous spheres. Good qualitative agreement was obtained for the two distinct flame structures.

Jiang et al. (1995) analyzed numerically multiple flame configurations of a convective n-octane fuel droplet at various Damköhler and Reynolds numbers with 0.1 mm diameter. The gas flow field is predicted by solving the quasi-steady conservation equations of mass, momentum and energy, in which gas-phase combustion is modeled by a one-step global finite-rate chemical reaction. Multiple flame configurations were obtained under the quasi-steady prediction presented. The solutions were in qualitative agreement with previous calculations and experimental studies.

Pope e Gogos (2005) investigated a n-heptane fuel droplet extinction due to forced

convection with numerical simulation for droplet sizes ranging from 0.1 mm to 15 mm and a wide range of ambient temperatures. The gas-phase solution was obtained using the quasi-steady equations of mass, momentum, species, and energy conservation. Numerical predictions were in quantitative agreement with experimental data available in the literature. As previously said, a linear dependence of the extinction velocity as a function of droplet diameter constitutes the present state of knowledge. Pope e Gogos (2005) predicted a nonlinear dependence for small droplet diameters (d < 1 mm) and a linear dependence only for large diameters (d > 2 mm). These results support the need for experiments with large droplets in microgravity.

Raghavan et al. (2005) simulated the combustion of a spherical fuel particle burning in a mixed convective environment both numerically and experimentally. The simulations were carried out at atmospheric pressure for various particle sizes, free-stream velocities and ambient temperatures. In the numerical model, transient axi-symmetric Navier-Stokes equations along with species and energy conservation equations are solved using a finite volume technique based on non-orthogonal semi-collocated grids. The numerical prediction was compared with the porous sphere experiment demonstrating good agreement. The results showed that, at higher ambient temperatures, transition to wake flame is delayed to a higher critical Reynolds number value.

More recently, Farouk e Dryer (2012) studied numerically the extinction characteristics of methanol droplet combustion under microgravity over a wide range of operating conditions and droplet sizes ranging from 1.5 mm to 7 mm. An "extinction characteristic" correlation was proposed that depends on burning rate, ambient diffusivity and flame standoff ratio. The flame standoff ratio is the ratio between the radial position of the flame and the droplet radius. Methanol droplet experiments conducted onboard of the International Space Station were found to yield results that agree well with the proposed "extinction characteristic" correlation.

2.4.3 Theoretical Studies

Fachini (1999) presented an analytical, steady state, droplet combustion model with considerations of temperature dependence of transport coefficients and non-unity Lewis number. Although the model admits these considerations, the results do not have good agreement with experimental results. The principal point is that the chemical reaction is to be considered one-step, which leads to an overestimation of flame temperature and, consequently, also the vaporization rate and the flame position.

Ackerman e Williams (2005) developed an asymptotic model for droplet combustion in a slow convective flow valid for small Reynolds number regime. The model was analyzed in terms of the Peclet number based on the Stefan velocity (the radial velocity of the gas at the surface of the droplet), taken to be of unity order, for Lewis numbers of unity order and for small values of a parameter ε, defined as the ratio of the convective velocity far from the droplet to the Stefan

velocity. The prediction that the burning-rate constant increases linearly with ε for small values of ε is shown to be consistent with available experimental data.

Recently, Ulzama e Specht (2007) presented a mathematical model for droplet combustion under microgravity conditions based on the fact that this process is controlled by both the quasi-steady and transient behavior. In this consideration the droplet combustion can be described by both quasi-steady behavior for the region between the droplet surface and the flame interface, and transient behavior for the region between the flame interface and ambient surrounding. When comparing of the modeling results with experimental data, it was observed that the simplified quasi-steady transient approach towards droplet combustion yielded behavior similar to the classical droplet theory.

2.5 Work Outline

The remaining chapters of the work are organized as follows. In chapter 2, the formulation implemented on this work is described. The mathematical formulation is presented with the dimensionless variables and governing equations for mass, momentum, energy and mixture fractions. The Shvab-Zel'dovich formulation is implemented and the boundary conditions are specified for droplet surface, inflow, outflow, side stream and symmetrical axis regions. The numerical solution is detailed, showing the solution sequence and the computational grid utilized. In chapter 3, the results showed are the mesh resolution independence for temperature and mixture fractions, a comparative between the numerical and analytic solutions, the gas-phase streamlines surrounding the droplet for normal and zero gravity, and an analysis of the influence of the ambient temperature on the variables distribution along inflow, center and outflow. The flame position is presented with the temperature field, also for different ambient temperatures. Finally, Chapter 4 includes the concluding remarks.

3 FORMULATION

3.1 Mathematical Formulation

In the present work, the physical model considers a porous sphere (named droplet) with liquid fuel being fed from its interior to its surface. The droplet is placed in a oxidizing environment under normal gravity $g = 9.8\ m/s^2$. The combustion process is represented by a one-step global reaction model of the form

$$F + sO_2 \rightarrow (1+s)P + q \tag{3.1}$$

where a mass s of oxidant is consumed per unit mass of fuel to yield a mass (1+s) of products and thermal energy q.

The schematic diagram of computation domain is shown in Fig. 7, in which the velocity V_n of vapor fuel injection normal to droplet surface is considered as a constant. The equations are described in cartesian coordinates. Compared to spherical coordinates the cartesian representation of Navier-stokes equation has simpler form and, consequently is easier to discretize, determine boundary contitions and to obtain a numerical solution.

Figure 7 – Problem schematic (constant radius droplet with fuel injection).
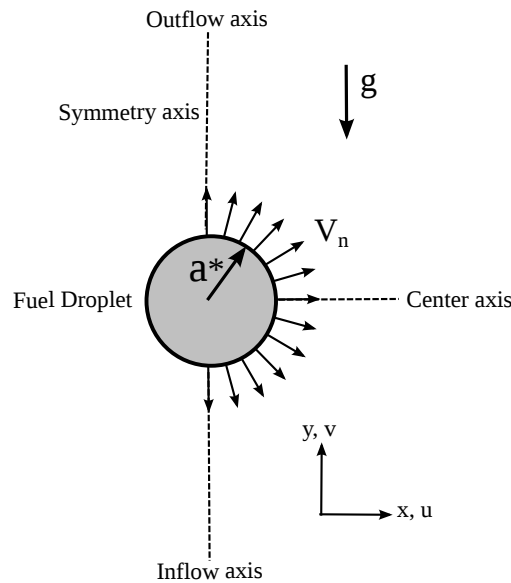
Source: The author.

The thermo-physical properties μ dynamic viscosity, k thermal diffusivity, $\mathscr{D}_i$ mass diffusivity of i species, and c_p specific heat are considered constant. The governing equations in incompressible form include the conservation equations for mass, momentum in horizontal and

vertical directions, mixture fractions of i species and energy:

$$\frac{\partial u^*}{\partial x^*} + \frac{\partial v^*}{\partial y^*} = 0 \tag{3.2}$$

$$\rho^* \left(\frac{\partial u^*}{\partial t^*} + \frac{\partial (u^* u^*)}{\partial x^*} + \frac{\partial (u^* v^*)}{\partial y^*} \right) = +\mu \left(\frac{\partial^2 u^*}{\partial x^{*2}} + \frac{\partial^2 u^*}{\partial y^{*2}} \right) - \frac{\partial P^*}{\partial x^*} \tag{3.3}$$

$$\rho^* \left(\frac{\partial v^*}{\partial t^*} + \frac{\partial (v^* u^*)}{\partial x^*} + \frac{\partial (v^* v^*)}{\partial y^*} \right) = +\mu \left(\frac{\partial^2 v^*}{\partial x^{*2}} + \frac{\partial^2 v^*}{\partial y^{*2}} \right) - \frac{\partial P^*}{\partial y^*} - \rho^* g \tag{3.4}$$

$$\rho^* \left(\frac{\partial Y_i^*}{\partial t^*} + \frac{\partial (u^* Y_i^*)}{\partial x^*} + \frac{\partial (v^* Y_i^*)}{\partial y^*} \right) = \rho^* \mathscr{D}_i \left(\frac{\partial^2 Y_i^*}{\partial x^{*2}} + \frac{\partial^2 Y_i^*}{\partial y^{*2}} \right) - s_i^* \dot{W}^* \tag{3.5}$$

$$\rho^* c_p \left(\frac{\partial T^*}{\partial t^*} + \frac{\partial (u^* T^*)}{\partial x^*} + \frac{\partial (v^* T^*)}{\partial y^*} \right) = k \left(\frac{\partial^2 T^*}{\partial x^{*2}} + \frac{\partial^2 T^*}{\partial y^{*2}} \right) + Q^* \dot{W}^* \tag{3.6}$$

in which the subscript represent $i = F$ for fuel and $i = O$ for oxidant and $\dot{W}^* = \rho^* B Y_O{}^{v_1} Y_F{}^{v_2} e^{-E/(RT^*)}$.

In the momentum equation, the local static pressure P may be broken down into two terms: one, P_a, due to the hydrostatic pressure, and other other, P_d, the dynamic pressure due to the motion of the fluid (i.e., $P = P_a + P_d$) (BEJAN; KRAUS, 2003). The former pressure component, coupled with the body force acting on the fluid, constitutes the buoyancy force that is the driving mechanism for the flow. If ρ_∞ is the ambient fluid density, the buoyancy term is written as $- \bigtriangledown P^* - \rho^* g = - \bigtriangledown P_d^* - g(\rho^* - \rho_\infty^*)$. The incompressible formulation is extensively used to simulate physical problems in the low Mach number condition and can be applicable to non-reacting flows at low speed (where the density is assumed to be constant) or in many combustion applications, where density is assumed to depend only on temperature gradients (LAW, 2006). Thus the density variation is only important in the buoyancy term.

The Boussinesq approximation is the most simple way to solve natural convection flow, without having to solve for the full compressible formulation of the Navier-Stokes equations. Thus, the buoyancy force $g(\rho_\infty^* - \rho^*)$ is replaced with $g \beta \rho^* (1 - T_\infty^*)$ with the density treated as constant (BEJAN; KRAUS, 2003) and β is a compressibility coefficient. This approximation reduces the nonlinearity of the problem. However this approximation is valid for small temperature or density differences.

In the present derivation the buoyancy force is obtained by the isobaric approximation, $g(\rho_\infty - \rho) \approx g/(T_\infty - T)$, which is not restricted to small temperature or density differences.

Then the Eq.3.4 becomes:

$$\rho^* \left(\frac{\partial v^*}{\partial t^*} + \frac{\partial (v^* u^*)}{\partial x^*} + \frac{\partial (v^* v^*)}{\partial y^*} \right) = +\mu \left(\frac{\partial^2 v^*}{\partial x^{*2}} + \frac{\partial^2 v^*}{\partial y^{*2}} \right) - \frac{\partial P_d^*}{\partial y^*} + \frac{g}{T_\infty - T} \tag{3.7}$$

in which ρ^* is a constant.

3.1.1 Adimensionalization

To reduce the number of variables and to be independent of system of unit, the equations are expressed in dimensionless form. All lengths are scaled with the initial droplet radius and the time is non-dimensionalized using gas-phase mass diffusion scale at the ambient conditions.

Thus dimensionless variables used in the analysis are defined as

$$T \equiv \frac{T^*}{T_\infty^*}, \quad Y_F \equiv Y_F^*, \quad Y_O \equiv \frac{Y_O^*}{Y_{O\infty}^*}, \quad x \equiv \frac{x^*}{a^*}, \quad y \equiv \frac{y^*}{a^*}, \quad u \equiv \frac{u^*}{v_c^*}, \quad v \equiv \frac{v^*}{v_c^*}, \quad P \equiv \frac{P^*}{P_c^*}, \quad t \equiv \frac{t^*}{t_c^*}$$

The superscript "*" stands for variables in dimensional form and the subscript b stand for boiling condition and ∞ stand ambient condition (far from the droplet). The variables T, ρ, Y_F, Y_O are temperature, density, fuel mass fraction, oxidant mass fraction, respectively. The cartesian coordinates, x and y, are nondimensionalized by the constant droplet radius a^*, the time t^* is estimated by heating time $t_c^* = a^{*2}/\alpha_\infty^* \varepsilon$, in which $\varepsilon \equiv \rho_\infty^*/\rho_l^*$, the subscript l stand for liquid phase. The velocity is nondimensionalized by the diffusion velocity of gas-phase $v_c^* \equiv \alpha_\infty/a^*$, α_∞ is the thermal diffusivity $\alpha_\infty = k_\infty/c_p \rho_\infty^*$. The pressure P^* is nondimensionalized by the characteristic pressure $P_c^* = \rho_\infty^* v_c^{*2}$.

The cartesian coordinates (x, y) are used in the formulation of the problem. The governing equations include the conservation equations for mass, momentum in the horizontal and vertical directions, energy and mixture fractions:

$$\frac{\partial u}{\partial x} + \frac{\partial v}{\partial y} = 0 \tag{3.8}$$

$$\frac{\partial u}{\partial t} + \frac{\partial u^2}{\partial x} + \frac{\partial (uv)}{\partial y} = +Pr \left(\frac{\partial^2 u}{\partial x^2} + \frac{\partial^2 u}{\partial y^2} \right) - \frac{\partial P_d}{\partial x} \tag{3.9}$$

$$\frac{\partial v}{\partial t} + \frac{\partial (vu)}{\partial x} + \frac{\partial v^2}{\partial y} = +Pr \left(\frac{\partial^2 v}{\partial x^2} + \frac{\partial^2 v}{\partial y^2} \right) - \frac{\partial P_d}{\partial y} + \frac{1}{Fr^2} \left(1 - \frac{1}{T} \right) \tag{3.10}$$

$$\frac{\partial T}{\partial t} + \frac{\partial (uT)}{\partial x} + \frac{\partial (vT)}{\partial y} = \frac{\partial^2 T}{\partial x^2} + \frac{\partial^2 T}{\partial y^2} + Q\dot{W} \tag{3.11}$$

$$\frac{\partial Y_i}{\partial t} + \frac{\partial (uY_i)}{\partial x} + \frac{\partial (vY_i)}{\partial y} = \frac{1}{Le_i}\left(\frac{\partial^2 Y_i}{\partial x^2} + \frac{\partial^2 Y_i}{\partial y^2}\right) - s_i\dot{W} \tag{3.12}$$

The dimensionless parameters $F_r = v_c^*/\sqrt{ga^*}$, $P_r = v_\infty/\alpha_\infty$ and $Le_i = \alpha_\infty/\mathscr{D}_{i\infty}$ are Froude, Prandtl and Lewis for the i species numbers, respectively, in which $i = F$ for fuel and $i = O$ for oxidant and v is the viscosity. Q is the rate of heat added by heat source and $\dot{w}_i = S_i\rho D_a Y_O{}^{v_1}Y_F{}^{v_2}e^{-\Sigma/T}$ is the net rate of work done on fluid element by surroundings. Where $D_a = Ba_0^{*2}Y_{O\infty}^{v_1}/\alpha_\infty$ is the dimensionless Damköhler number.

3.1.2 Shvab-Zel'dovich Formulation

A major difficulty in the solution of chemically reacting flows is the presence of the reaction term, which is not only nonlinear but also couples the energy and species equations, Eq. 3.11 and 3.12. However, recognizing that the concentrations of Y_F and Y_O species and the system enthalpy are related through stoichiometry, it is reasonable to expect that under suitable situations these quantities can be stoichiometrically combined such that the resulting term is not affected by chemical reactions in the flow. Such a combined quantity is called a coupling function (LAW, 2006).

To couple the energy and species equations, the Shvab-Zel'dovich formulation is applied and the assumption of an " infinitely rapid chemical reaction rate" is made. In this model the flame zone is of infinitesimal thickness and is represented by a surface rather than an extended reaction zone. In this model the Lewis number of i species is considered equal to unity. The goal of this formulation is to transform the system of three equations, Eq. 3.11 for energy and Eq. 3.12 for fuel and oxidant, in two linear equations as functions of Z and H, representing the fraction of mixture and excess enthalpy, respectively. Combining Eq. 3.11 and 3.12:

$$\frac{\partial}{\partial t}\left\{\begin{array}{c} T \\ Y_O \\ Y_F \end{array}\right\} + \frac{\partial}{\partial x}\left\{\begin{array}{c} uT \\ uY_O \\ uY_F \end{array}\right\} + \frac{\partial}{\partial y}\left\{\begin{array}{c} vT \\ vY_O \\ vY_F \end{array}\right\} =$$

$$\frac{\partial^2}{\partial x^2}\left\{\begin{array}{c} T \\ Y_O/Le_O \\ Y_F/Le_F \end{array}\right\} + \frac{\partial^2}{\partial y^2}\left\{\begin{array}{c} T \\ Y_O/Le_O \\ Y_F/Le_F \end{array}\right\} + \left\{\begin{array}{c} Q \\ -s_O \\ -s_F \end{array}\right\}\dot{W} \tag{3.13}$$

Knowing that $s_F = 1$, multiplying the second line by Le_O and the third by Le_F in Eq. 3.13:

$$\frac{\partial}{\partial t} \left\{ \begin{array}{c} T \\ Le_O Y_O \\ Le_F Y_F \end{array} \right\} + \frac{\partial}{\partial x} \left\{ \begin{array}{c} uT \\ Le_O u Y_O \\ Le_F u Y_F \end{array} \right\} + \frac{\partial}{\partial y} \left\{ \begin{array}{c} vT \\ Le_O v Y_O \\ Le_F v Y_F \end{array} \right\} =$$

$$\frac{\partial^2}{\partial x^2} \left\{ \begin{array}{c} T \\ Y_O \\ Y_F \end{array} \right\} + \frac{\partial^2}{\partial y^2} \left\{ \begin{array}{c} T \\ Y_O \\ Y_F \end{array} \right\} + \left\{ \begin{array}{c} Q/Le_F \\ -s_O Le_O/Le_F \\ -1 \end{array} \right\} \dot{W} Le_F \quad (3.14)$$

Multiplying the third line by $S = s_O Le_O/Le_F$ and subtracting the second line:

$$\frac{\partial}{\partial t}(Le_F S Y_F - Le_O Y_O) + \frac{\partial}{\partial x}[u(Le_F S Y_F - Le_O Y_O)] +$$

$$\frac{\partial}{\partial y}[v(Le_F S Y_F - Le_O Y_O)] = \frac{\partial^2}{\partial x^2}(S Y_F - Y_O) + \frac{\partial^2}{\partial y^2}(S Y_F - Y_O) \quad (3.15)$$

Adding a unitary constant on the terms inside the derivatives:

$$\frac{\partial}{\partial t}[(Le_F S Y_F - Le_O Y_O + 1)] + \frac{\partial}{\partial x}[u(Le_F S Y_F - Le_O Y_O + 1)] +$$

$$\frac{\partial}{\partial y}[v(Le_F S Y_F - Le_O Y_O + 1)] = \frac{\partial^2}{\partial x^2}(S Y_F - Y_O + 1) + \frac{\partial^2}{\partial y^2}(S Y_F - Y_O + 1) \quad (3.16)$$

Defining mixture fraction by $Z = S Y_F - Y_O + 1$ and $Le_O = Le_F = 1$:

$$\frac{\partial Z}{\partial t} + \frac{\partial(uZ)}{\partial x} + \frac{\partial(vZ)}{\partial y} = \frac{\partial^2 Z}{\partial x^2} + \frac{\partial^2 Z}{\partial y^2} \quad (3.17)$$

where $S \equiv v_O/y_{O\infty}$, v_O is the mass of oxidant consumed for each unit of mass of fuel in the condition of stoichiometric reaction.

Multiplying the first line in Eq. 3.13 for $((S+1)Le_F/Q)$ and adding to the second and third line:

$$\frac{\partial}{\partial t}\left(\frac{(S+1)Le_F}{Q}T + Le_F Y_F + Le_O y_O\right) + \frac{\partial}{\partial x}\left[u\left(\frac{(S+1)Le_F}{Q}T + Le_F Y_F + Le_O y_O\right)\right] +$$

$$\frac{\partial}{\partial y}\left[v\left(\frac{(S+1)Le_F}{Q}T + Le_F Y_F + Le_O y_O\right)\right] =$$

$$\frac{\partial}{\partial x}\left[\frac{\partial}{\partial x}\left(\frac{(S+1)Le_F}{Q}T + Y_F + y_O\right)\right] + \frac{\partial}{\partial y}\left[\frac{\partial}{\partial y}\left(\frac{(S+1)Le_F}{Q}T + Y_F + y_O\right)\right] \quad (3.18)$$

Defining the enthalpy excess $H = (S+1)Le_F T/Q + y_O + y_F$:

$$\frac{\partial H}{\partial t} + \frac{\partial (uH)}{\partial x} + \frac{\partial (vH)}{\partial y} = \frac{\partial^2 H}{\partial x^2} + \frac{\partial^2 H}{\partial y^2} \tag{3.19}$$

where $Q \equiv Q^*/(c_{p\infty}T_\infty^*)$ is the dimensionless heat combustion.

The general Shvab-Zel'dovich formulation (Eqs. 3.17 and 3.19) describes the temperature and the oxygen and fuel mass fractions by determining the mixture fraction and the enthalpy excess functions in the fuel region and in the oxygen region. In the present model, is assumed that the combustion process occurs under condition of Damköhler number infinitely large ($D_a \gg 1$). In other words, the reaction characteristic time is infinitely smaller than any mechanical characteristic time. Thus, the reactants can not coexist, i.e., the flow field is divided in two domains separated by a reaction sheet. In the fuel droplet region $Y_O = 0$ the oxygen concentration is zero. In the oxygen domain, $Y_F = 0$. Both reactants have zero concentration at the flame, where the chemical reaction takes place.

In order to obtain an equation to describe the temperature profile, the enthalpy excess and mixture fraction were combined resulting the following expression:

$$T(Z,H) = \begin{cases} \frac{Q(H-(Z-1)/S)}{(S+1)Le_F}, & \text{for} \quad Z > 1 \\[2mm] \frac{Q(H-Z-1)}{(S+1)Le_F}, & \text{for} \quad Z \leq 1 \end{cases} \tag{3.20}$$

In a similar way, the mass fraction is obtained through the mixture fraction distribution:

$$Y_i(Z) = \begin{cases} \frac{Z-1}{S}, & \text{for} \quad Z > 1 \\[2mm] 1-Z, & \text{for} \quad Z \leq 1 \end{cases} \tag{3.21}$$

3.1.3 Boundary Conditions for $g \neq 0$

With reference to Fig. 8, the following conditions have been specified at the boundaries:
Droplet surface: $(x^2 + (y-y_c)^2 \approx a)$

At the droplet surface, the Dirichlet boundary conditions for all variables are imposed as follows:

$$u_s = \frac{|\vec{V}_n|x}{r}, \quad v_s = \frac{|\vec{V}_n|(y-y_c)}{r}, \quad Z_s = S+1, \quad H_s = (S+1)\frac{T_s}{Q} + 1, \quad P_s = P_\infty + \frac{\rho_s|\vec{V}_n|^2}{2} \tag{3.22}$$

in which the subscript "s" stands for condition at the droplet surface, $r = \sqrt{x^2 + (y-y_c)^2}$, y_c stands for the vertical distance between the origin of the domain and the center of the droplet

radius. Remembering that, $\vec{V}_n$ is the injection velocity of the fuel normal to the droplet surface. If all flow is inviscid and follows streamlines normal to the boundaries, Bernoulli's can be used to derive boundary condition for the pressure under inflow and outflow conditions, as described above.

Figure 8 – Computational Domain.
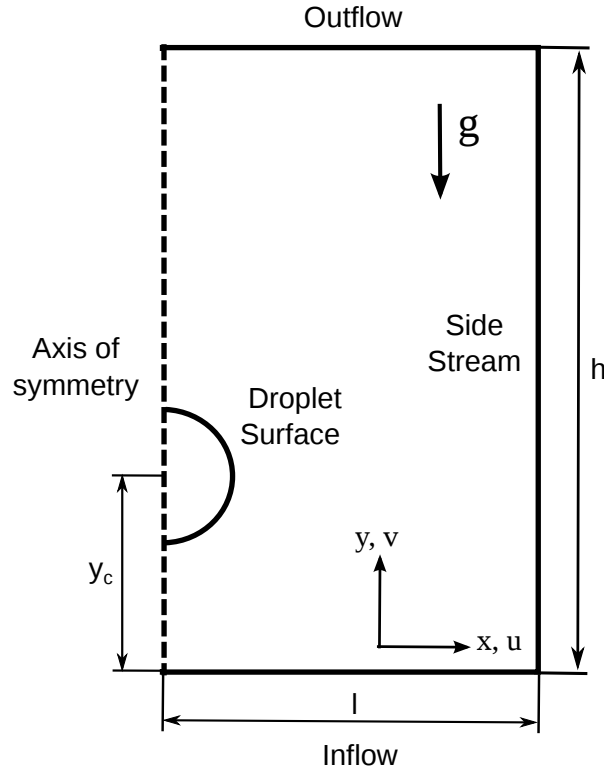
Source: The author.

Inflow freestream: $(0 \leq x \leq l)$ at $y = 0$

The bottom of domain is characterized as inflow condition due the effect of buoyancy force that moves the hot gases of the flame upwards, inducing air from the bottom of domain upwards. Thus the boundary conditions placed at 30 times the droplet radius are defined as follows:

$$\left.\frac{\partial u}{\partial y}\right|_{y=0} = \left.\frac{\partial v}{\partial y}\right|_{y=0} = 0, \quad Z_\infty = 0, \quad H_\infty = (S+1)\frac{T_\infty}{Q} + 1, \quad P = P_\infty \tag{3.23}$$

Note that the variable mixture fraction $Z = 0$ means $Y_o = 1$ (pure oxidant) and the condition freestream (subscript ∞ stands for condition far from the droplet) allow to impose temperature and pressure conditions prescribed

Outflow freestream: $(0 \leq x \leq l)$ at $y = h$

In the outflow boundary condition the normal derivatives of all variables are set to zero at the boundary, which means that the variables do not change in the direction normal to the boundary.

$$\left.\frac{\partial u}{\partial y}\right|_{y=h} = \left.\frac{\partial \mathrm{v}}{\partial y}\right|_{y=h} = \left.\frac{\partial Z}{\partial y}\right|_{y=h} = \left.\frac{\partial H}{\partial y}\right|_{y=h} = \left.\frac{\partial P}{\partial y}\right|_{y=h} = 0 \qquad (3.24)$$

This boundary condition makes physical sense under condition of boundary far away from high gradients. In the present model, the outflow boundary condition is placed at 90 times the droplet radius.

Axis of symmetry: $x = 0$ for $0 \leq y \leq h$

$$u = 0, \quad \frac{\partial \mathrm{v}}{\partial x} = \frac{\partial Z}{\partial x} = \frac{\partial H}{\partial x} = \frac{\partial P}{\partial x} = 0 \qquad (3.25)$$

Right side freestream: $x = l$ for $0 \leq y \leq h$

$$\left.\frac{\partial u}{\partial x}\right|_{x=l} = \left.\frac{\partial \mathrm{v}}{\partial x}\right|_{x=l} = 0, \quad Z_\infty = 0, \quad H_\infty = (S+1)\frac{T_\infty}{Q} + 1, \quad P = P_\infty \qquad (3.26)$$

the boundary condition right side freestream is placed at 50 times droplet radius.

3.1.4 Boundary Conditions for $g = 0$

To simulate numerically the droplet combustion in a zero gravity environment the following boundary conditions are applied:

Droplet surface:

$$u = \frac{|\vec{V}_n|x}{r}, \qquad \mathrm{v} = \frac{|\vec{V}_n|(y - y_c)}{r} \qquad (3.27)$$

$$H = (S+1)\frac{T_s}{Q} + 1, \qquad Z = S+1, \quad P_s = P_\infty + \frac{\rho_s|\vec{V}_n|^2}{2} \qquad (3.28)$$

in which the subscript "s" stands for condition at the droplet surface, $r = \sqrt{x^2 + (y - y_c)^2}$, y_c stands for the vertical distance between the origin of the domain and the center of the droplet radius.

Inflow freestream ($0 \leq x \leq L$ at $y = 0$), Right side freestream ($x = L$ for $0 \leq y \leq H$) and Outflow freestream ($0 \leq x \leq L$ at $y = H$):

$$\frac{\partial u}{\partial n} = \frac{\partial \mathrm{v}}{\partial n} = 0, \qquad \frac{\partial Z}{\partial n} = \left[\frac{(S+1)}{1 - e^{-\dot{m}}}\right]\frac{\dot{m}}{r^2}, \qquad \frac{\partial H}{\partial n} = \frac{1}{r^2}, \quad P = P_\infty \qquad (3.29)$$

where n is the normal coordinate, y for inflow and outflow freestream boundaries and x for right side freestream boundary. It is important to notice here that the boundaries inflow and right side freestream kept their names only for convention, in $g = 0$ case they are treated as a outflow freestream boundary condition.

Axis of symmetry: $x = 0$ for $0 \le y \le H$

$$u = 0, \quad \frac{\partial v}{\partial x} = \frac{\partial Z}{\partial x} = \frac{\partial H}{\partial x} = \frac{\partial P}{\partial x} = 0 \tag{3.30}$$

3.2   Analytical solution for spherically symmetric droplet combustion ($g = 0$)

The quasi- steady model of sphero-symmetric combustion of a droplet has been extensively studied, analytically as well as numerically (GOLDSMITH, 1954; KASSOY; WILLIAMS, 1968; WILLIAMS, 1985; PURI; LIBBY, 1991; FACHINI, 1999). The mathematical model and assumptions described in Section 2.1 are used to depict analytically the combustion phenomenon of isolated pure fuel droplet under microgravity condition. The problem is described by the spherical uni-dimensional conservation equations of mass, energy and species:

$$\frac{1}{r^2} \frac{\partial}{\partial r} (r^2 \rho u) = 0 \tag{3.31}$$

$$\frac{1}{r^2} \frac{\partial}{\partial r} \left(r^2 \rho u \left\{ \begin{array}{c} T \\ Y_O \\ Y_F \end{array} \right\} \right) = \frac{1}{r^2} \frac{\partial}{\partial r} \left(T^n r^2 \frac{\partial}{\partial r} \left\{ \begin{array}{c} T \\ Y_O \\ Y_F \end{array} \right\} \right) + \left\{ \begin{array}{c} Q \\ -s \\ -1 \end{array} \right\} \dot{W} \tag{3.32}$$

In which r is the droplet radius Integrating Eq. A.1:

$$r^2 \rho u = \dot{m} \tag{3.33}$$

where $\dot{m} = M / a_0^2 u_c$.

Combining Eqs. A.2 yield the general Shvab-Zel'dovich formulation

$$\dot{m} \frac{\partial Z}{\partial r} = \frac{\partial}{\partial r} \left(r^2 \frac{\partial Z}{\partial r} \right) \tag{3.34}$$

$$\dot{m} \frac{\partial H}{\partial r} = \frac{\partial}{\partial r} \left(r^2 \frac{\partial H}{\partial r} \right) \tag{3.35}$$

The boundary conditions for Eqs. A.6 and A.7 are

$$Z(1) = S + 1, \qquad\qquad Z(\infty) = 0 \tag{3.36a}$$

$$H(1) = \frac{(S+1)}{Q} T_b + 1, \qquad H(\infty) = \frac{(S+1)}{Q} T_\infty + 1 \tag{3.36b}$$

Applying the operations showed in Appendix A, the final equations to describe mixture fractions and enthalpy in a symmetric droplet combustion are defined as follow

$$Z = \frac{S+1}{1-e^{-\dot{m}}}\left(1 - e^{\left(-\frac{\dot{m}}{r}\right)}\right) \tag{3.37}$$

$$H = H(\infty)e^{\left(-\frac{\dot{m}}{r}\right)} + \left(\frac{H(1) - H(\infty)e^{-\dot{m}}}{1 - e^{-\dot{m}}}\right)\left(1 - e^{\left(-\frac{\dot{m}}{r}\right)}\right) \tag{3.38}$$

As in the numerical case, the temperature is computed from enthalpy and mixture fraction through the Eq. 3.20.

3.3 Numerical Solution for $g = 9,81m/s^2$

The momentum equations were discretized by the quadratic upstream interpolation for convective kinetics (QUICK) scheme. This high order differencing scheme, presented by Leonard (1979), uses a three-point upstream-weighted quadratic interpolation for cell face values. This scheme was selected for its stability, sensitivity to the flow direction, third-order truncation error and effectiveness for steady or quasi-steady flows (FLETCHER, 2012).

Considering the two-dimensional control volume schematized on Fig. 9, the discretization of Eq. 3.9 and 3.10 can be summarized as

$$a_P\phi_P = a_W\phi_W + a_E\phi_E + a_S\phi_S + a_N\phi_N$$
$$+ a_{WW}\phi_{WW} + a_{EE}\phi_{EE} + a_{SS}\phi_{SS} + a_{NN}\phi_{NN} + S \tag{3.39}$$

with central coefficient

$$a_P = a_W + a_E + a_S + a_N + a_{WW} + a_{EE} + a_{SS} + a_{NN} + F_e - F_w + F_n - F_s \tag{3.40}$$

and neighbor coefficients

$$a_W = D_w + \frac{6}{8}\alpha_w F_w + \frac{1}{8}\alpha_e F_e + \frac{3}{8}(1 - \alpha_w)F_w \tag{3.41}$$

$$a_{WW} = -\frac{1}{8}\alpha_w F_w \tag{3.42}$$

$$a_E = D_e - \frac{3}{8}\alpha_e F_e - \frac{6}{8}(1 - \alpha_e)F_e - \frac{1}{8}(1 - \alpha_w)F_w \tag{3.43}$$

$$a_{EE} = \frac{1}{8}(1 - \alpha_e)F_e \tag{3.44}$$

$$a_S = D_s + \frac{6}{8}\alpha_s F_s + \frac{1}{8}\alpha_n F_n + \frac{3}{8}(1-\alpha_s)F_s \tag{3.45}$$

$$a_{SS} = -\frac{1}{8}\alpha_s F_s \tag{3.46}$$

$$a_N = D_n - \frac{3}{8}\alpha_n F_n - \frac{6}{8}(1-\alpha_n)F_n - \frac{1}{8}(1-\alpha_s)F_s \tag{3.47}$$

$$a_{NN} = \frac{1}{8}(1-\alpha_n)F_n \tag{3.48}$$

Figure 9 – Control Volume.
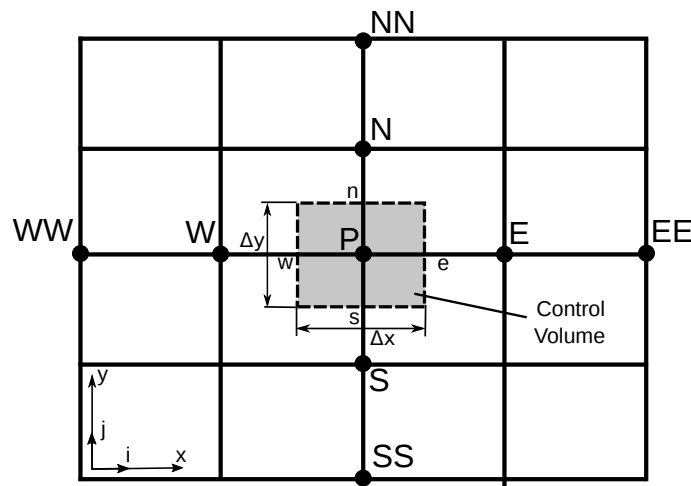
Source: The author.

where

$$\alpha_w = 1 \quad for \quad F_w > 0, \quad \alpha_e = 1 \quad for \quad F_e > 0$$

$$\alpha_s = 1 \quad for \quad F_s > 0, \quad \alpha_n = 1 \quad for \quad F_n > 0$$

$$\alpha_w = 0 \quad for \quad F_w < 0, \quad \alpha_e = 0 \quad for \quad F_e < 0$$

$$\alpha_s = 0 \quad for \quad F_s < 0, \quad \alpha_n = 0 \quad for \quad F_n < 0$$

The variable F represents the convective mass flux per unit area and D the diffusion conductance at cell faces. The term S represents the source term of buoyancy and pressure.

3.3.1 The Artificial Compressibility Method

The artificial compressibility method evolved from density-based methods, that were developed for transonic and supersonic compressible flows. The principle of the artificial compressibility method lies in the introduction of an artificial compressibility parameter δ_c into the continuity equation and an artificial state equation $p = \rho_c / \delta_c$, where ρ is the artificial density (CHORIN, 1967). Thus

$$\delta_c \frac{\partial p}{\partial t} + \frac{\partial u}{\partial x} + \frac{\partial \mathrm{v}}{\partial y} = 0 \tag{3.49}$$

where t is an auxiliary variable whose role is analogous to that of time in a compressible flow problem. Thus the present model is valid only for steady-state solution. The parameter δ_c is a disposable parameter, analogous to a relaxation parameter, which enables the system of Eq.3.49, Eq.3.9 and Eq.3.10 to converge to a solution that satisfies the incompressibility condition.

The above system also has similarities with the equations of motion for a compressible fluid at low Mach numbers. Making this analogy, the artificial compressibility parameter can be related to an artificial speed of sound $c = 1/\sqrt{\delta_c}$.

The use of the artificial compressibility method results in a system of a hyperbolic-type equations of motion. Waves of finite speed are introduced into the incompressible flow field as a medium to distribute the pressure. The speed of propagation of these pseudo waves depends on the magnitude of the artificial compressibility parameter δ_c. Ideally, the value of δ_c is to be chosen so that the speed of the introduced waves approaches that of the incompressible flow. This, however, introduces a problem of contaminating the accuracy of the numerical algorithm, as well as affecting its stability. On the other hand, if δ_c is chosen such that these waves travel too slowly, then the variation of the pressure field accompanying these waves is very slow. Therefore, a method of controlling the speed of pressure waves and their interactions with the vorticity spreading is key to the success of this approach.

3.3.2 Computational Grid

To prevent possible pressure oscillations, it was used an uniform structured staggered grid, in which the pressure p is located in the cell centers, the horizontal velocity u in the midpoints of the vertical cell edges, and the vertical velocity v in the midpoints of the horizontal cell edges, as showed in Fig. 10. Consequently, not all the extreme grid points come to lie on the boundary domain. The vertical boundaries, for instance, carry no v-values, just as the horizontal boundaries carry no u-values. For this reason, an extra boundary strip of grid cells is introduced, so that the boundary conditions may be applied by averaging the nearest grid points on either side.

Figure 10 – Staggered grid.
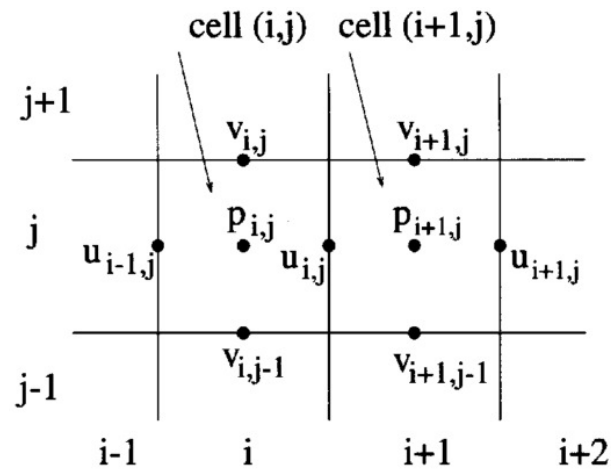
Source: The author.

To identify the fluid cells on the computational grid it is used an integer array, named FLAG, which can be initialized as follows:

- C_F for a fluid;

- C_B for an obstacle surface;

- C_BS for an fluid close to the obstacle surface;

- C_I for the interior of the obstacle.

The macros C_F, C_B, C_BS and C_I denote fixed integer constants which can be chosen arbitrarily.

Figure 11 – Grid regions representation.
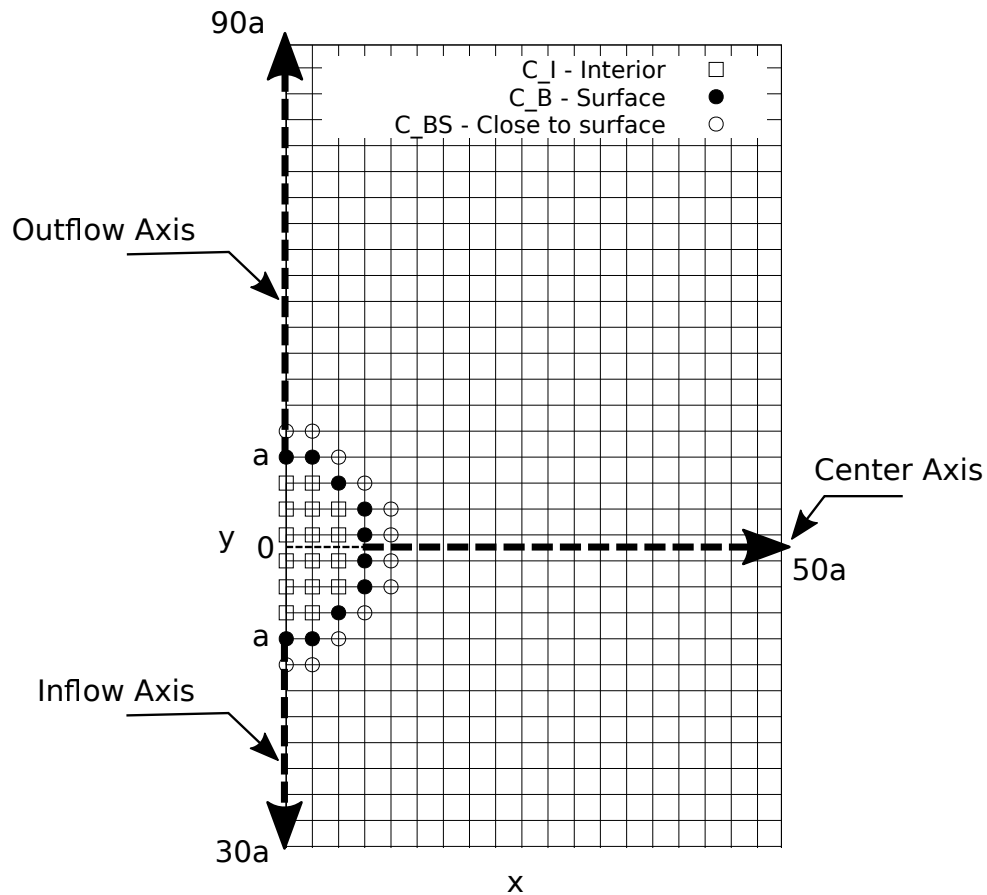
Source: The author.

3.3.3 Solution Procedure

To obtain a steady-state solution, an artificial explicit time-dependent marching scheme is employed in Eqs. 3.49, 3.9, 3.10, 3.17 and 3.19. The numerical solution follows the sequence:

1. Values of ambient condition for Z, H and P and zero velocity are provided as an initial condition;

2. A first estimative for velocity components u and v are obtained by Eqs. 3.9 and 3.10;

3. The pressure is obtained through mass conservation using the artificial compressibility method;

4. The mixture fraction Z, Eq. 3.17, provides the estimative for species y_F, y_O;

5. The temperature T is obtained by excess enthalpy H, Eq. 3.19, and mixture fraction Z;

6. The new estimative for velocity components is obtained by the input of the old temperature and pressure as sources;

7. Finally, this numerical procedure is recursively repeated until: (1) the solution reaches the steady state, that is, the artificial compressibility term on mass conservation has fully vanished; (2) the following global convergence criteria is satisfied: For $\phi_{i,j} \geq \phi^{max} \times 10^{-3}$,

$$\left| \frac{\phi_{i,j} - \phi_{i,j}^{prev}}{\phi_{i,j}} \right| \leq 1.0 \times 10^{-4}, \tag{3.50}$$

otherwise,

$$\left| \frac{\phi_{i,j} - \phi_{i,j}^{prev}}{\phi^{max} \times 10^{-3}} \right| \leq 1.0 \times 10^{-4}; \tag{3.51}$$

where ϕ can be u, v, P, Z and H; the superscript (prev) indicates the value at the previous iteration; and ϕ^{max} is the maximum variable value in the given phase. Equation 3.51 was included to allow convergence when velocities near zero exist in the computational domain (POPE; GOGOS, 2005).

The solution methodology outlined above has been implemented using a FORTRAN code and computations have been carried out on a personal computer with Intel® Core™ i7-4500U CPU @ 1.80GHz × 4 processor. For most of cases, the time step is $dt = 5 \times 10^{-5}$ and $dt = 1 \times 10^{-4}$ for test cases . Each computation required about 12h to have a converged solution and obtain enough iterations to reach the steady state solution.

4 RESULTS AND DISCUSSION

4.1 Mesh Resolution, Domain and Convergence Verification

A verification of the code was made in order to determine if the numerical implementation accurately represents a conceptual description of the model and the solution of the model (OBERKAMPF; TRUCANO, 2002). In the present work the strategy of verification consists of doing some tests: mesh independence, independence of domain size and comparison between numerical and analytical solutions under the condition of microgravity.

The following results are presented along the axes named as inflow axis, center axis and outflow axis, as indicated in Fig. 11.

Figures 12 and 13 show the temperature and mass fraction of species for three regions of the domain with different mesh resolutions. Discrepancies are more significant in the outflow region. The mesh analysis indicated a significant mesh dependency until 197×475 in this region, as showed on Figs. 12c and 13c. The outflow region should take more attention, because it is where the rise of the high temperature plume from the flame is located, making its solution difficult. From these results it was selected the 197×475 mesh for all the next simulation cases.

Figure 12 – Test mesh dependence: Temperature profile for (a) inflow, (b) center and (c) outflow axes.
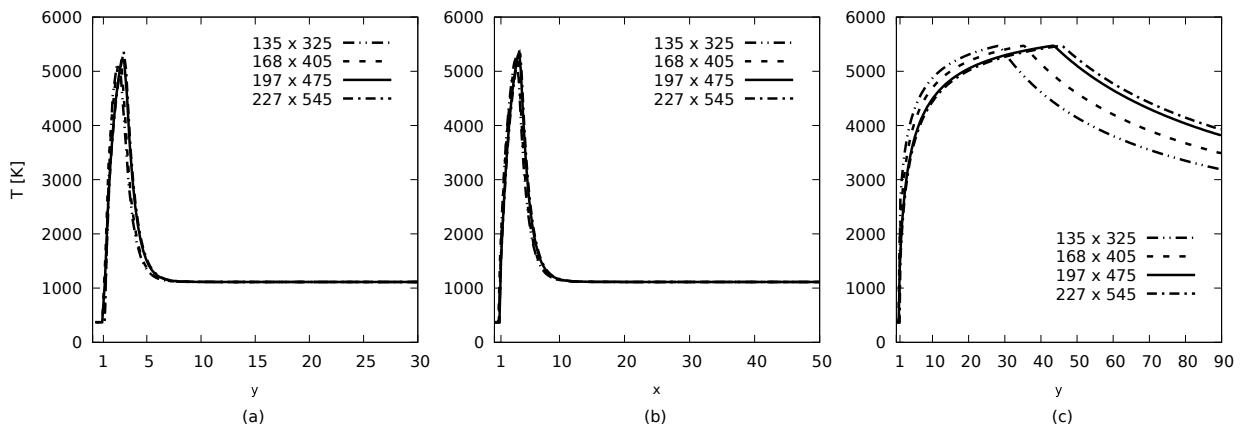
Source: The author.

Figure 13 – Test mesh dependence: Mass fraction for (a) inflow, (b) center and (c) outflow axes.
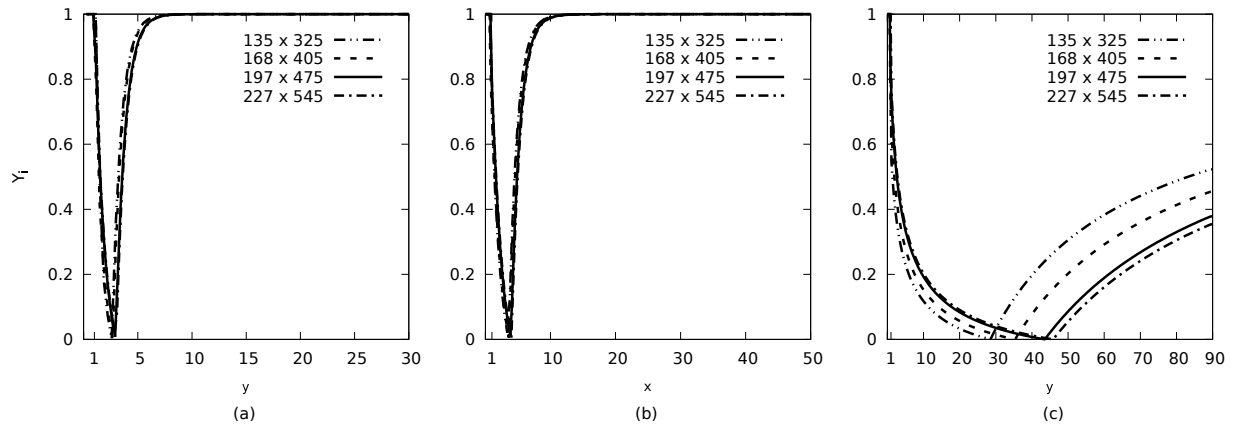
Source: The author.

Figures 14 and 15 show the temperature profile and mass fraction distribution for two different domain sizes. The mesh resolution was linked with the domain size to maintain the same Δx and Δy respecting the previous mesh analysis. The comparison demonstrates that the numerical solution is not significantly influenced by the domain size. However, the required time for the solution to reach convergence triplicated with $l = 100$ - $h = 200$ domain. The domain with length $l = 50$ and height $h = 120$ was selected for all next simulations because during the simulation the flame can not approach of the outflow boundary (top of domain).

Figure 14 – Dependence of domain size: Temperature for (a) inflow, (b) center and (c) outflow axes.
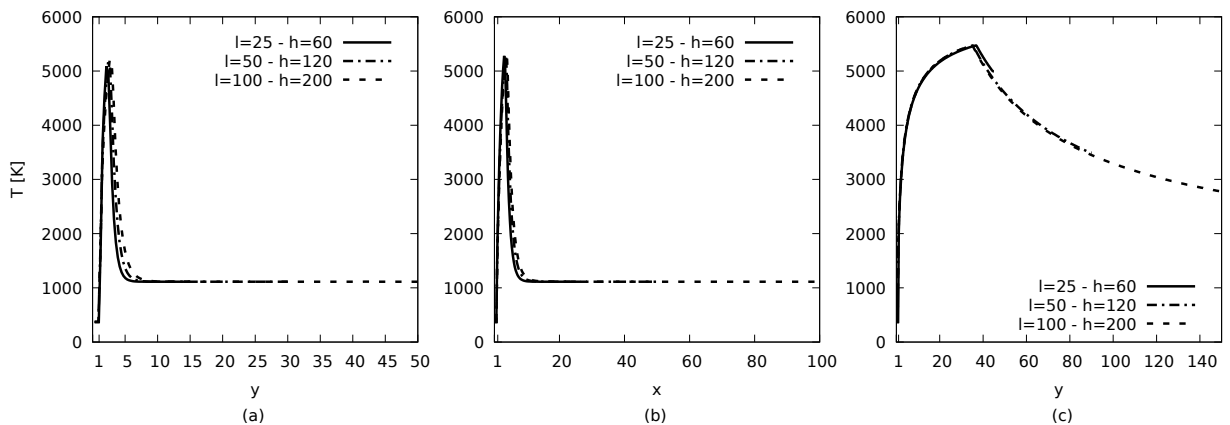

Source: The author.

Figure 15 – Dependence of domain size: Mass Fraction for (a) inflow, (b) center and (c) outflow axes.
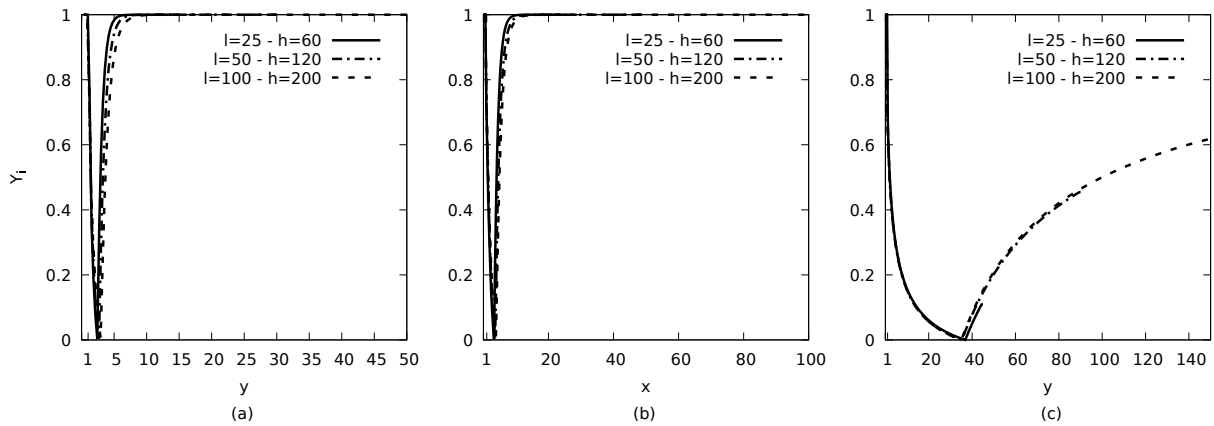
Source: The author.

Figure 16 shows the error evolution obtained from Eqs. 3.50 and 3.51 for velocities u and v and pressure P until the convergence criteria. It can be seen that the errors had two stages until its convergence. The first stage appeared because of the initial condition. It should be noted that the input is a spherical flame, similarly as in microgravity conditions, and zero velocity components in all directions. When the buoyancy source term starts to act, raising the hot gas from the flame region, the flame tip is elongated and reaches the outflow boundary. In this moment the error value increases considerably and starts to oscillate, this behavior is specified as the transition to Stage 2. On the Stage 2, the hot gas is expelled from the domain and a new flame tip is formed. From this moment on, the errors decrease, normally reaching its convergence criteria.

Figure 16 – Error evolution until convergence.
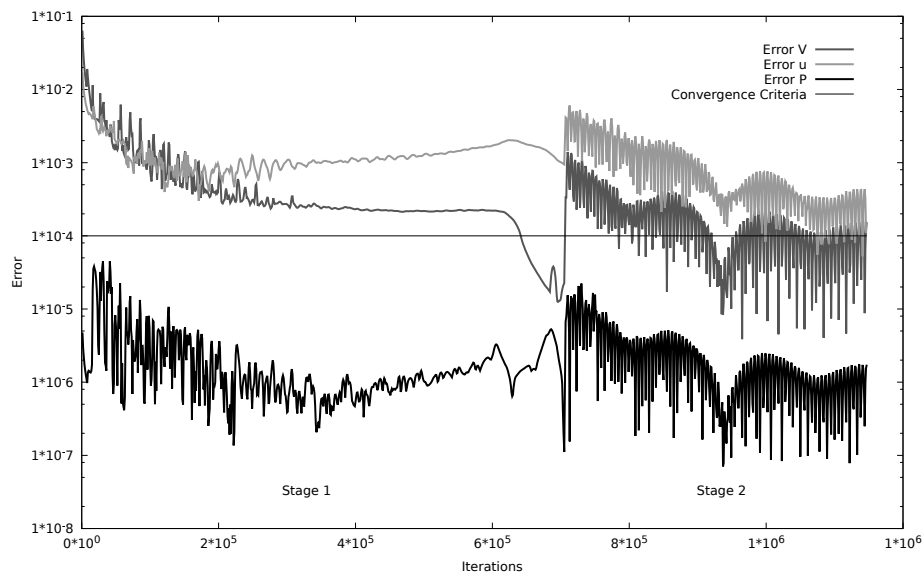
Source: The author.

4.2 Zero Gravity Code Verification

In a zero gravity environment there is no natural convection, and the steady flow is spherically symmetrical, dependent only on the radial coordinate. The analytic solution for droplet combustion was compared with the numerical solution. To simulate numerically the zero gravity conditions, the buoyancy source term was neglected in Eq. 3.10 and the boundary conditions presented on Section 3.2 were implemented on the numerical code.

Figure 17 compares the numerical and analytical solution results for temperature and mass fraction with the ambient temperature $T_\infty = 3T_b$. The agreement is reasonably favorable, with a small over-prediction in flame position, that is where the mass fraction has its null value. As showed in Fig. 17a and 17b, there is a good agreement of the predicted flame temperature and mass fraction distribution with the analytical solution.

Figure 17 – Comparison in the center axis for (a) Temperature and (b) Mass fraction .
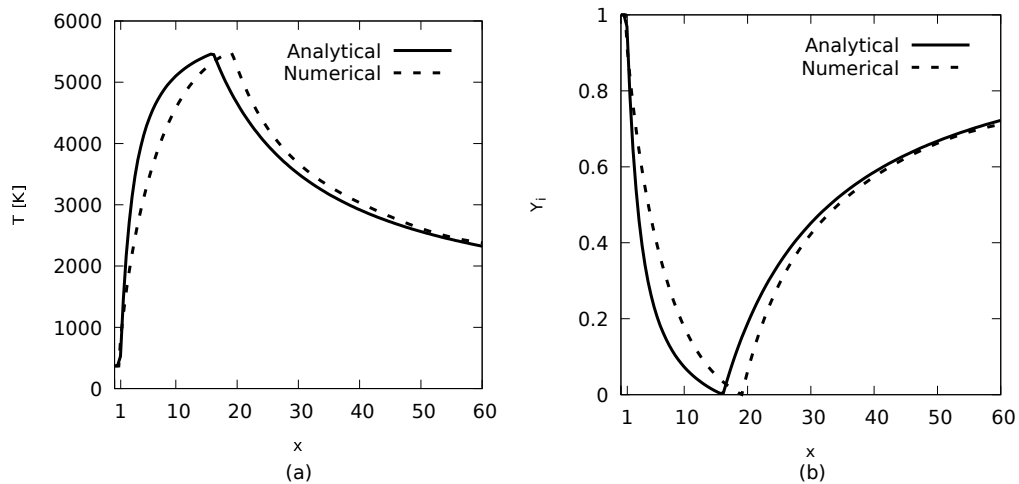
Source: The author.

4.3 Normal and Zero Gravity Conditions

Figures 18a and 18b show the gas-phase streamlines surrounding the droplet for $g = 9,81m/s^2$ and $g = 0m/s^2$ cases, respectively. The streamlines were generated through ParaView v5.0, an open-source analysis and visualization application. For the normal gravity case (Fig. 18a), flow directions are influenced by natural convection due to the presence of the buoyancy term in the conservation equation. Also shown in Fig. 18a is the stagnation point in the inflow region due to the relative flow direction opposing the fuel injection at droplet surface. In contrast, for the case without gravity, the buoyancy term is neglected and there is no natural convection acting in the flow field, resulting in a symmetrical flow.

Figure 18 – Streamlines for $T_\infty = 3T_b$: (a) $g = 9,81 m/s^2$ (b) $g = 0 m/s^2$.
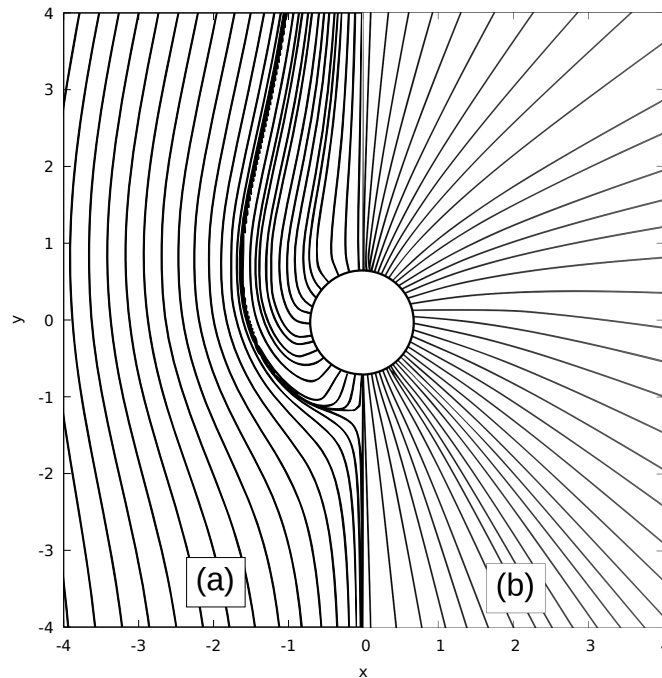
Source: The author.

Figures 19a and 19b are gray scale plots of the temperature distribution surrounding the droplet with normal and zero gravity condition, respectively. Both figures show trends similar to those of their corresponding streamline plots (Figs. 18a and 18b). The temperature distribution for normal gravity case (Fig.19a) shows a highly elongated flame in the outflow region. In contrast, the zero gravity environment (Fig. 19b) yields a spherically symmetric flame.

Figure 19 – Temperature field for $T_\infty = 3T_b$: (a) $g = 9,81 m/s^2$ (b) $g = 0 m/s^2$.
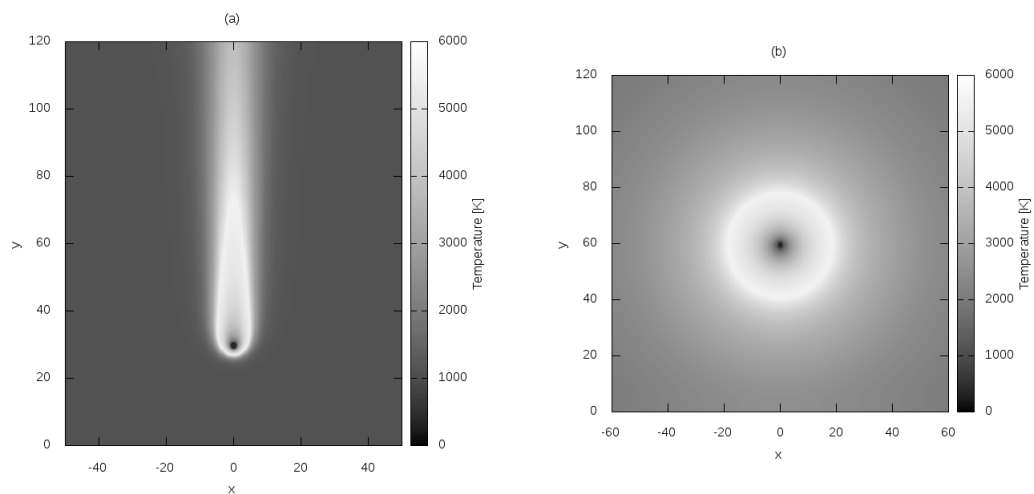

Source: The author.

4.4 Influence of Ambient Temperature

As stated in the introduction, one objective of this dissertation has been the analysis of the ambient temperature influence over the single droplet combustion under a natural convection environment. Several simulations with ambient temperature varying from $3T_b$ to $6T_b$ were carried out and compared to each other. In this section, all variables are analyzed in three main axis of interest, outflow, center and inflow, as showed in Fig. 7.

Figures 20a, 20b and 21 show the mixture fraction distribution along the inflow, center and outflow axis. Mixture fraction carries the physical meaning of the relative amounts of fuel and oxidizer at flow field. Thereby, it can be used to generate a mass fraction distribution. When Z is unity, fuel and oxidant are totally consumed, indicating the flame position. When Z is null, there is only oxidant, indicating ambient conditions. If $Z = s + 1 = 8,73$, there is only fuel, indicating droplet surface conditions.

Figure 20 – Mixture fraction distribution.

(a) Inflow   (b) Center
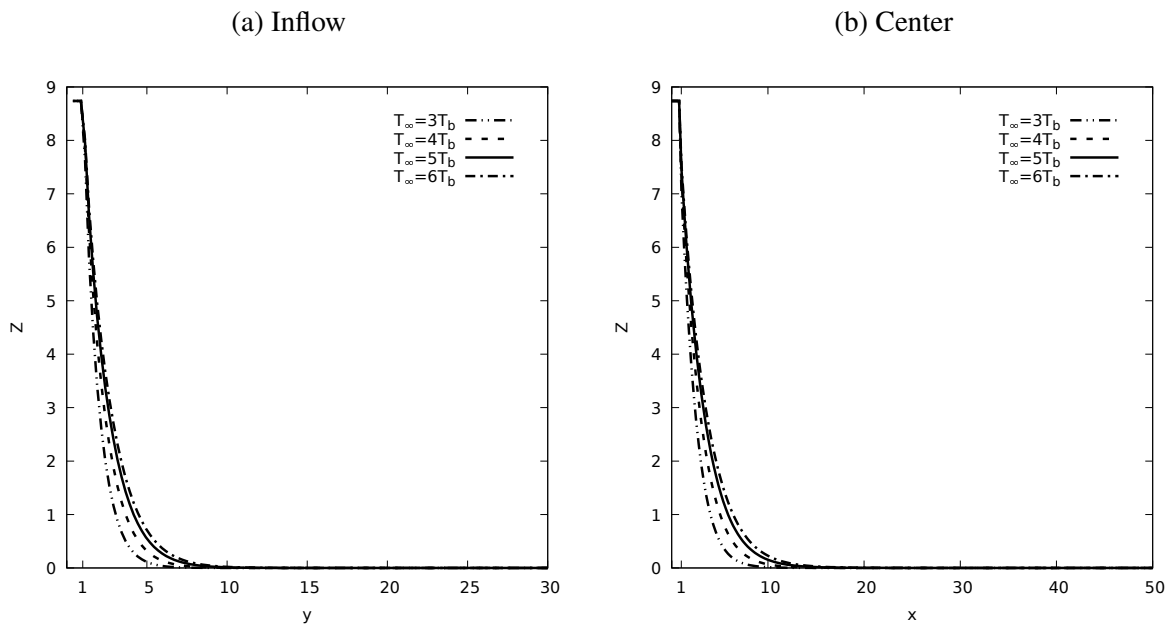
Source: The author.

It can be seen, from Figs. 20a and 20b, that the mixture fraction reaches ambient conditions around $y = 10$ in both regions. These results show that only oxidant exists until we reach the domain boundary. For the outflow region, Fig. 21 shows a different behavior. The mixture fraction reaches unity far from droplet surface and does not present null values, indicating that there are products of the combustion and not only oxidant in this region. For all axes, the mixture fraction curvature increases with the increase of ambient temperature, enlarging the flame.

Figure 21 – Mixture fraction distribution in the outflow axis.
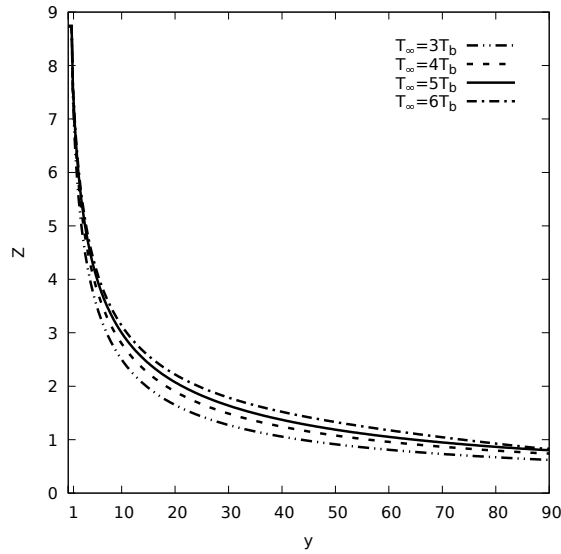
Source: The author.

Figures 22a, 22b and 23 show the enthalpy excess distribution along the inflow, center and outflow axes. As expected, the enthalpy excess increases with the increase of temperature in all analyzed axis due to its direct relation with a temperature ($H \equiv (S+1)Le_F T/Q + y_O + y_F$). The enthalpy excess at inflow and center axis have the same behavior, increasing their value until its maximum and then remains constant. This constant enthalpy excess corresponds to the ambient temperature, as expected, follows the same behavior.

Figure 22 – Enthalpy excess distribution.

(a) Inflow   (b) Center
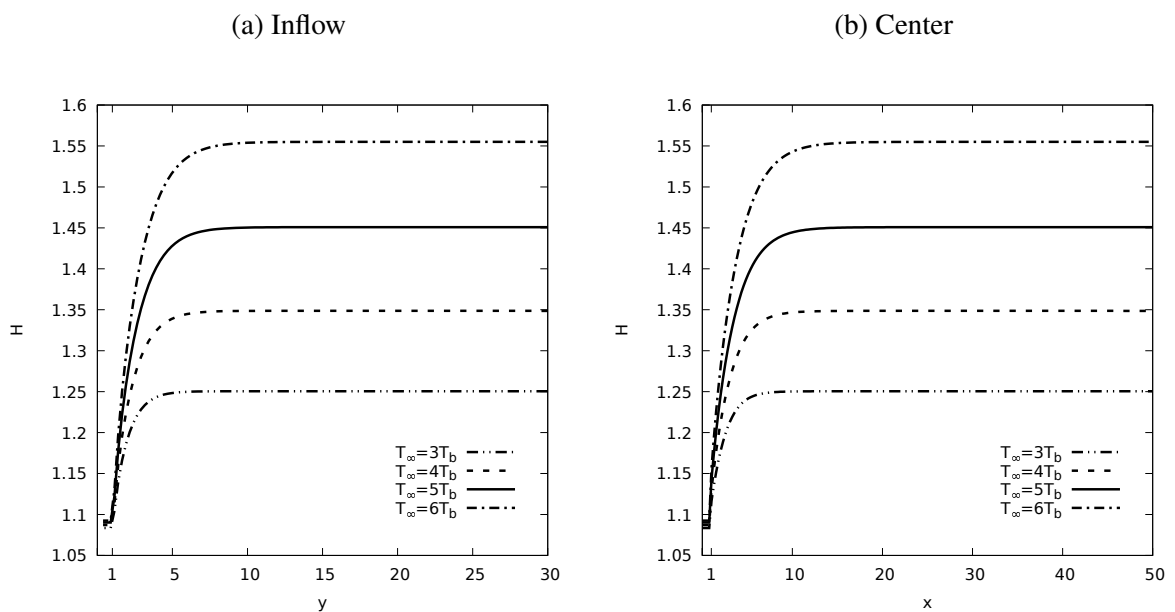
Source: The author.

In the distribution showed in Fig. 23, the enthalpy excess keeps increasing until the

outflow boundary. It should be noticed here that the temperature is computed from Z and H values. Thus, these enthalpy excess results with the previous mixture fraction results for outflow, outcomes in a higher temperature than the ambient temperature for this region.

Figure 23 – Enthalpy excess distribution in the outflow axis.
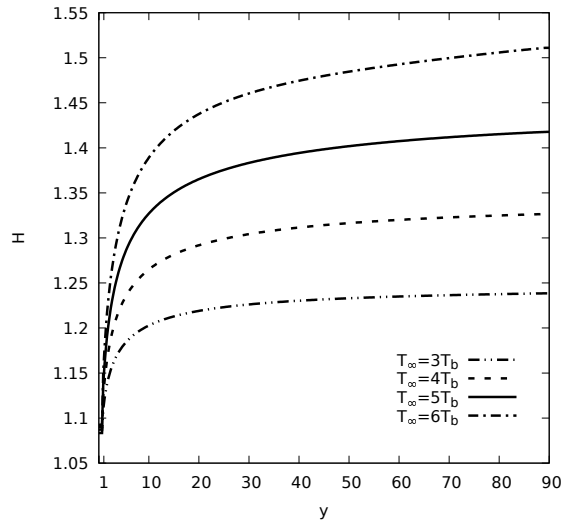
Source: The author.

Figure 24 – Mass fraction distribution.

(a) Inflow   (b) Center
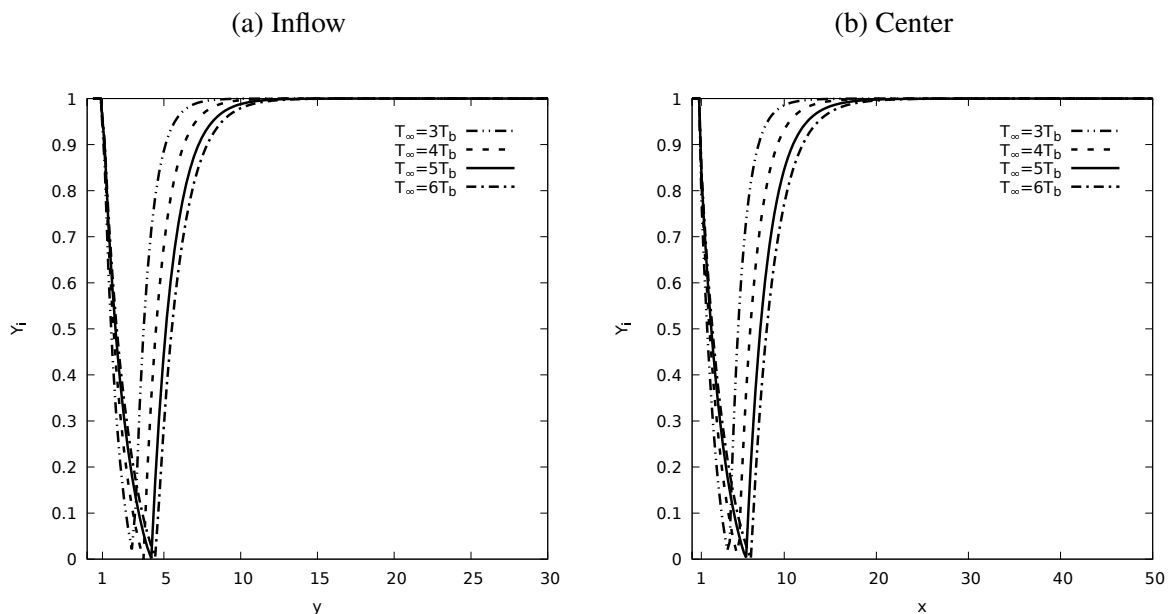
Source: The author.

Figures 24a, 24b and 25 show the mass fraction of fuel and oxidant, respectively, obtained by the solution of mixture fraction along the inflow, center and outflow axes. As expected the fuel and oxidant are totally consumed at flame position, and thereby there is no leakage of the

fuel and oxidizer across the reaction sheet. All axis show this classic diffusion-flame profile, with fuel being supplied from the droplet surface (left side, $Y_i = Y_F$) and oxidant entering from the ambient (right side, $Y_i = Y_O$), then Y_F and Y_O vanish in the right and left sides respectively. In the outflow axis, Fig. 25, the mass fraction of oxidant is lower than unity. Its can be explained due the flow of the combustion products in the outflow direction.

Figure 25 – Mass fraction distribution in the outflow axis.
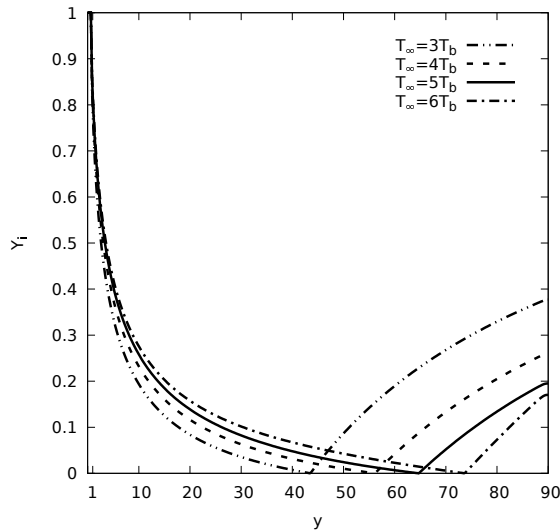
Source: The author.

Figure 26 – Temperature distribution.
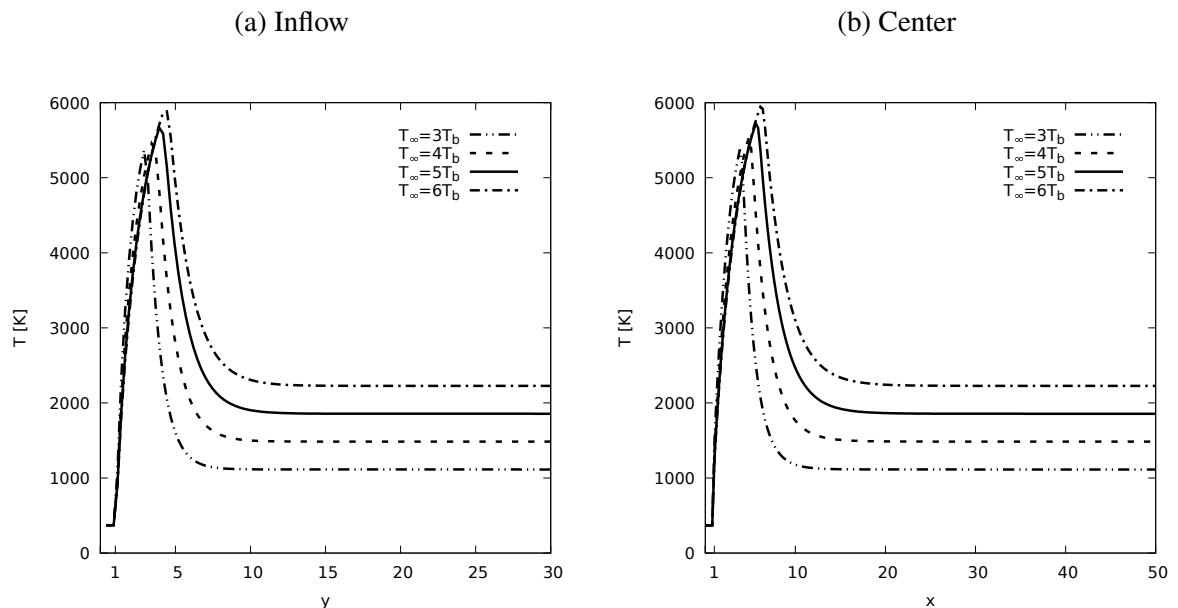
(a) Inflow

(b) Center

Source: The author.

Figures 26a, 26b and 27 show the dimensional temperature profile along the inflow, center and outflow axes, respectively, under different ambient temperature conditions. Along the inflow

and center axis (Figs. 26a and 26b), the temperature profile starts at *n*-heptane boiling temperature on surface, reaches its maximum value, characterized as the flame position, and decreases until reaching ambient temperature. It can be seen that the flame temperature and position depends on the ambient temperature. It should be notice that the predicted flame temperature is much higher than the adiabatic flame temperature for the *n*-heptane ($T_{ad} = 2290K$).

In the outflow region, the temperature reaches its maximum value and, in contrast to inflow and center behavior, a hot temperature plume is carried out to the boundary as shown in Fig. 27. Also in the outflow region, the dependence of the flame position to the ambient temperature is pronounced. This behavior can be explained by the fact that the temperature gradient in the flame decreases when ambient temperature increases, consequently, to achieve this condition the flame has to be more elongated.

Figure 27 – Temperature distribution in the outflow axis.
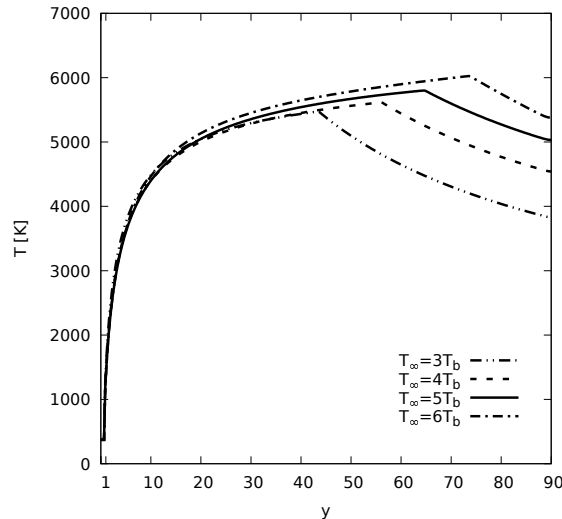
Source: The author.

Figures 28a, 28b and 29 show the buoyancy source term distribution along the inflow, center and outflow axes. As expected, the results show that the buoyancy term decreases with increasing the ambient temperature for all regions. The results also show that there is a negative buoyancy region around the droplet. For the inflow and center axes, Figs. 28a and 28b, the buoyancy term increases until its maximum value in the flame position and after decreases to a null constant value at the ambient. Since the local temperature is equal to the ambient temperature in these regions of the domain, this behavior was expected and agrees with the previous results for temperature distribution. In contrast, for the outflow axis (Fig. 29), the buoyancy term does not vanish, indicating a buoyant transport carrying the flow until the outflow freestream boundary. Again, this can be explained by the presence of a hot temperature plume above the flame position.

Figure 28 – Buoyancy source term distribution.
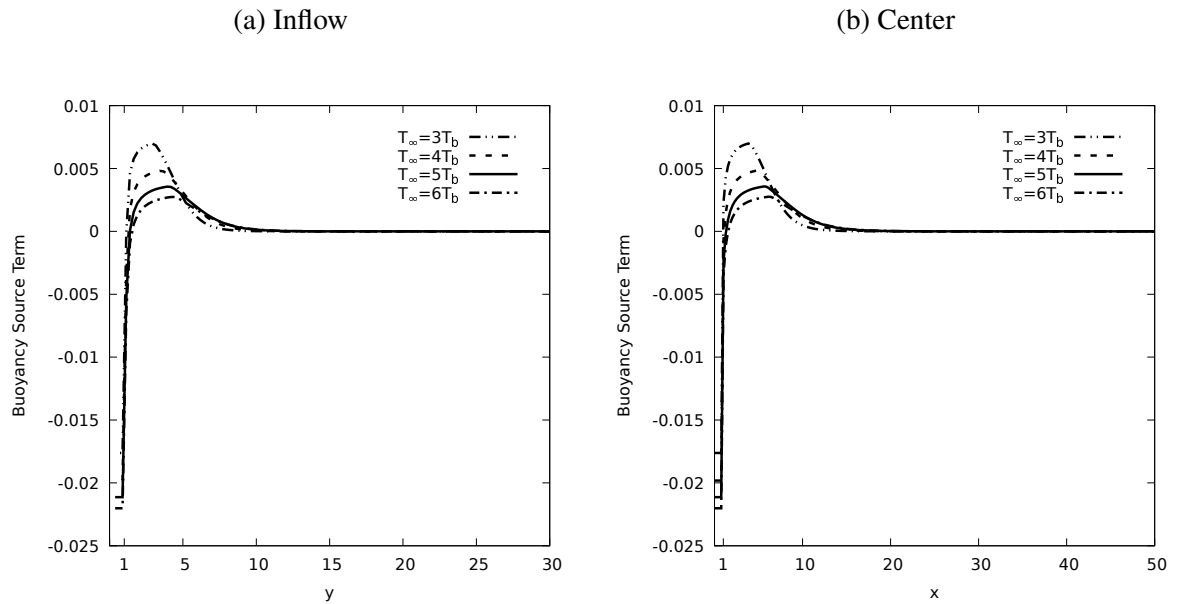
(a) Inflow

(b) Center

Figure 29 – Buoyancy source term distribution in the outflow axis.
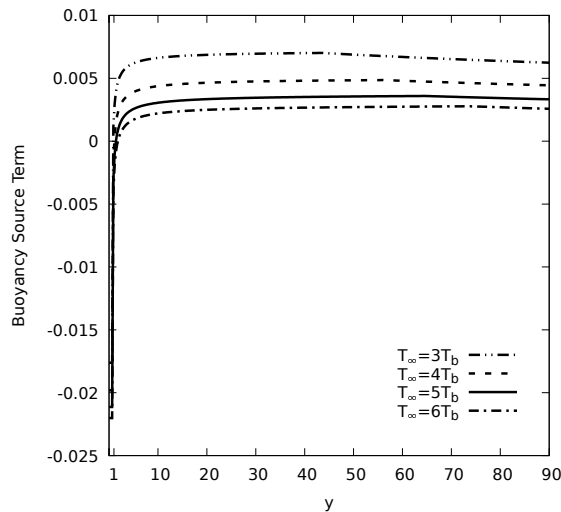
Figures 30a, 30b and 31 show the dimensionless absolute velocity distribution along the inflow, center and outflow axes. As expected, the flow velocity in the inflow decrease with the increase of the ambient temperature, as shown in Fig. 30a. Close to the droplet surface the velocity is null due to the stagnation point. The stagnation point is due to the injection of fuel at the droplet surface in the direction opposed to the flow induced by buoyancy force, as already stated in the streamlines analysis (Fig. 18). In the center region, the velocity close to the droplet decreases with the increasing ambient temperature. In the same region, far from the droplet the

velocity increases with the increase in ambient temperature. By the Fig. 30b, it can be seen that the velocity difference in the center axis decreases between close and far from the droplet. Figure 31 shows that in the outflow axis the absolute velocity decreases wile increasing the ambient temperature.

Figure 30 – Dimensionless absolute velocity distribution.
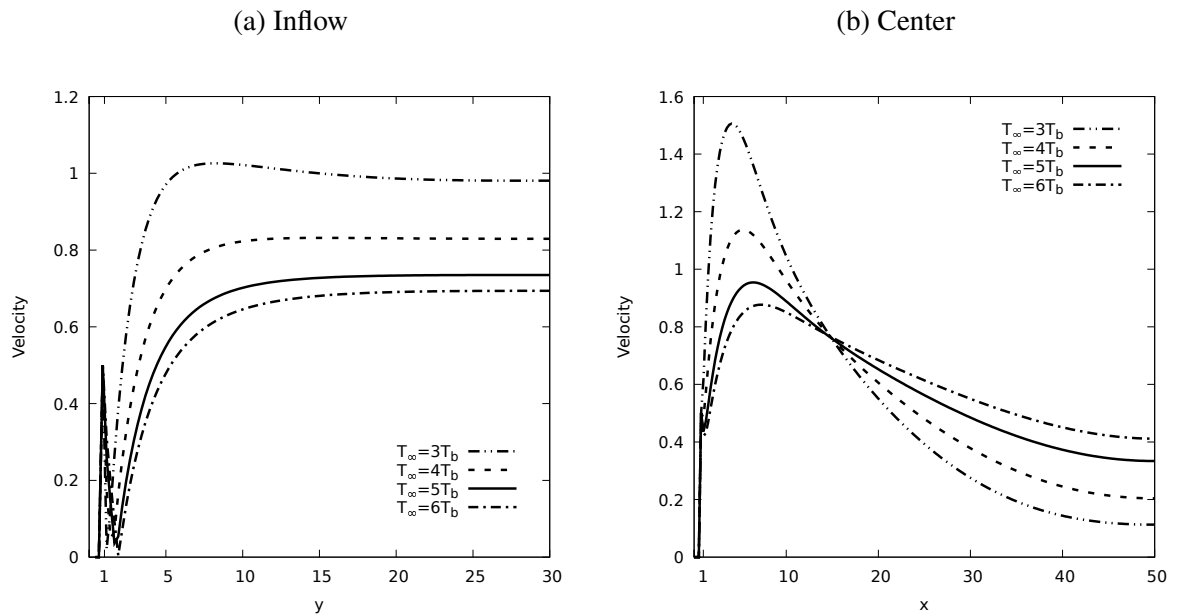
(a) Inflow

(b) Center

Source: The author.

Figure 31 – Dimensionless absolute velocity distribution in the outflow axis.
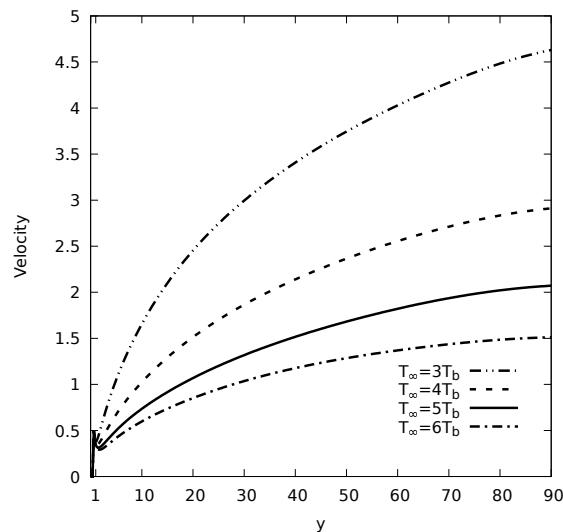

Source: The author.

Figures 32a, 32b and 33 show the dimensionless pressure distribution along the inflow, center and outflow axes. It can be seen that the pressure gradient decreases with the increase in

ambient temperature, indicating a more homogeneous velocity distribution as showed in Figs. 30 and 31. Previous analysis of streamlines (Fig.18) has shown that to bypass the droplet injection flow, the flow raising from below has to change its direction below the droplet (inflow axis) and accelerate in center region. Thus, as showed in Fig. 32b, the pressure decreases in center axis and reaches ambient values close to the right side boundary. For the inflow axis, Fig. 32a shows that at the stagnation point the pressure rapidly increases its value and then decreases to an ambient value at the inflow boundary. At outflow axis, the pressure close to the droplet surface suddenly decreases and starts to increase until a value around the ambient pressure, as shown in Fig. 33.

Figure 34 compares the complete domain streamlines for two ambient temperature conditions. For the $T_\infty = 3T_b$ case, Fig. 34a shows a highly strained streamline distribution close to the axis of symmetry. The flow vectors enters from the inflow and side stream boundaries and accelerates close to the flame region due to the strong convection transport. This accelerated flow around the flame region pushes the low velocity flow that is close to the ambient, bending the streamlines, as clearly showed in Fig. 34a. For $T_\infty = 6T_b$, Fig. 34b shows a smoothly change in velocity direction. In this case, the buoyancy transport is less pronounced than in the previous case, resulting in a more homogeneous velocity distribution, showing concordance with the previous analysis in Fig. 30b.

Figure 32 – Dimensionless pressure distribution.

(a) Inflow   (b) Center
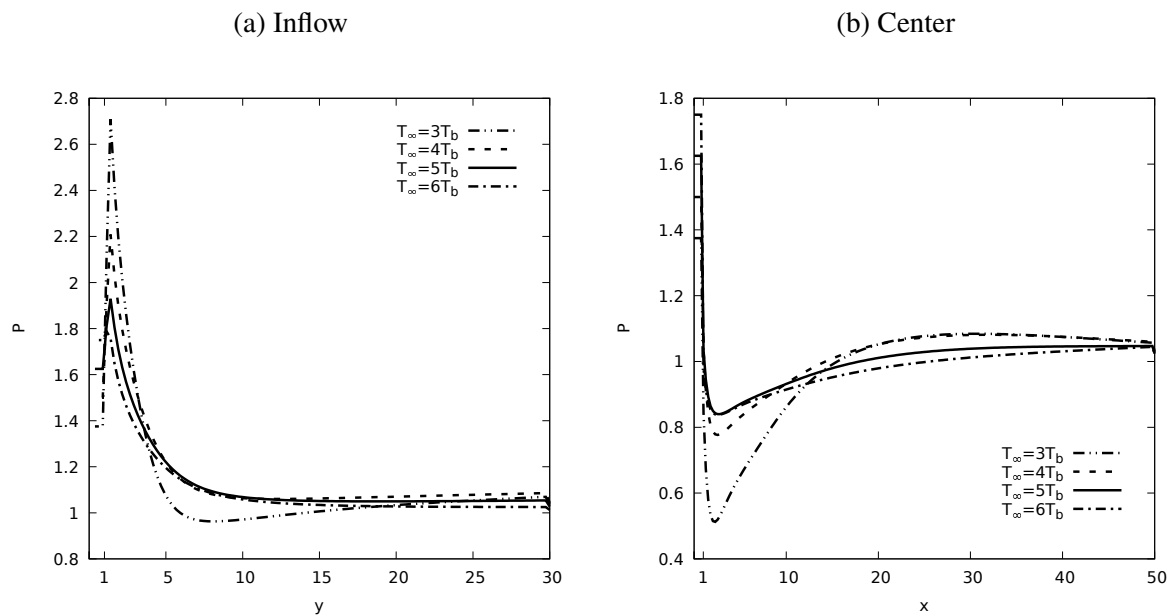
Source: The author.

Figure 33 – Dimensionless pressure distribution in the outflow axis.
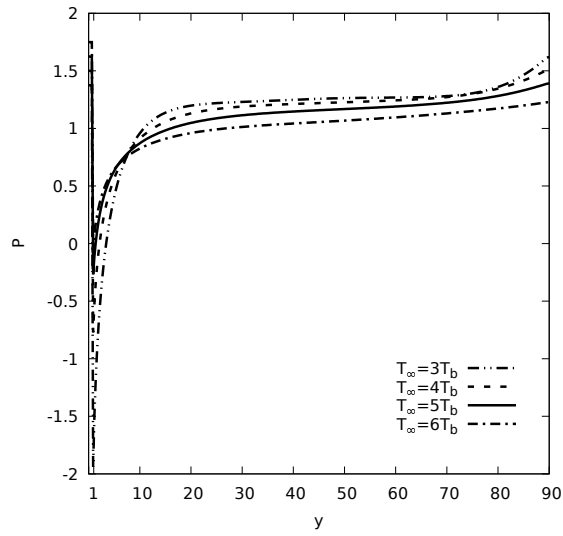
Source: The author.

Figure 34 – Complete domain streamlines for (a) $T_\infty = 3T_b$ and (b) $T_\infty = 6T_b$.
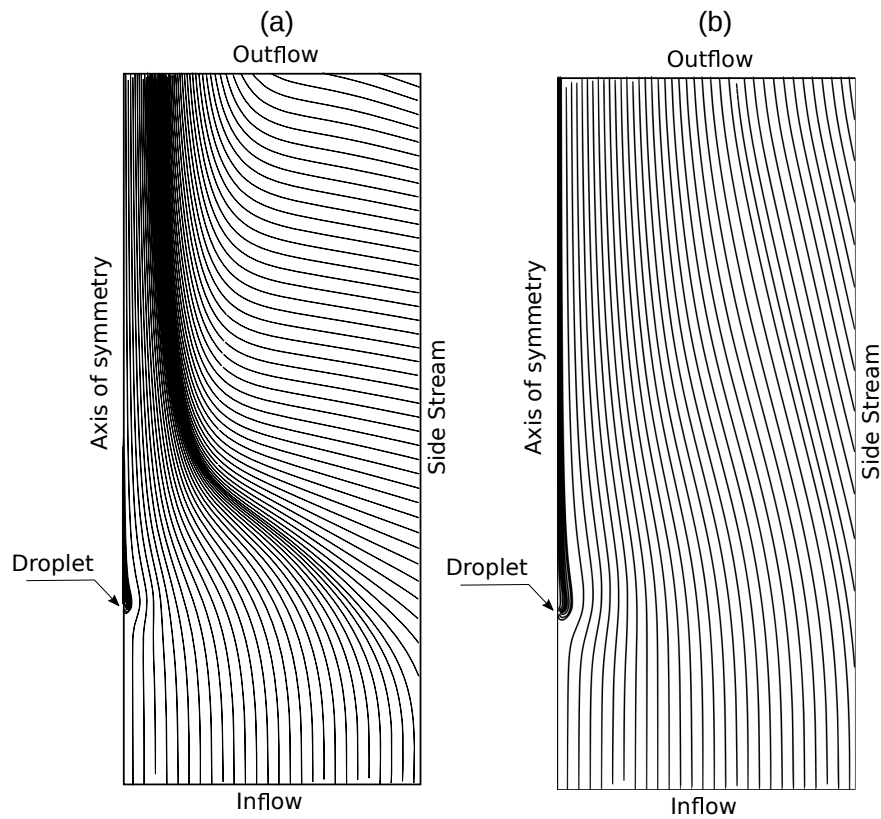
Source: The author.

4.5 Flame Shape Behavior

The flame shapes for a $1mm$ sphere burning in different ambient temperatures are shown in Fig. 35. The contour lines corresponding to stoichiometric value, that is the location when the mixture fraction reaches values above 1, have been used to delineate the flame surfaces in Fig. 35. The flame length and width to the center in both axes increases as the ambient temperature increases.

Figure 35 – Influence of ambient temperature on flame shape.
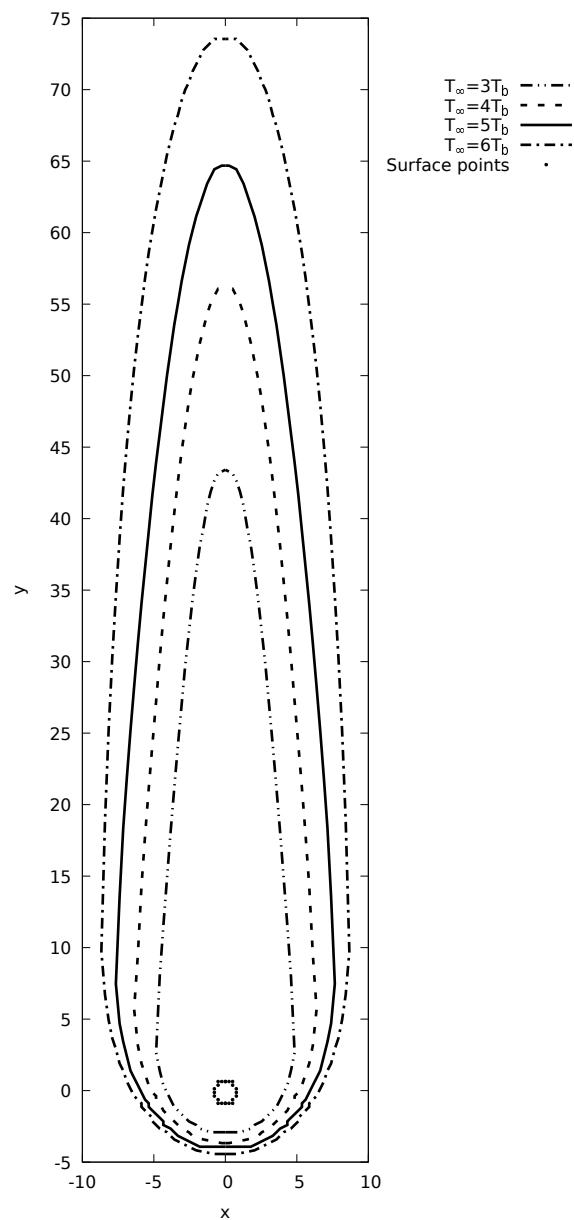
Source: The author.

Table 1 show the flame position values relative to Fig. 5. Analyzing the changing of dimensions, the results show that taking $T_\infty = 3T_b$ case as reference, all dimensions increased at

least half of their initial value. The flame width w_f increased two times its value from $T_\infty = 3T_b$ to $T_\infty = 6T_b$ cases, show that despite the flame height increased, the flame shape become more elliptic.

Table 1 – Flame dimensions.

	Flame Dimensions			**Increase (%)**		
T_∞	h_f	w_f	s_f	h_f	w_f	s_f
$3T_b$	43,41	8,16	2,91	ref.	ref.	ref.
$4T_b$	56,07	12,24	3,68	29,16	50	26,46
$5T_b$	64,68	14,28	3,93	48,99	75	35,05
$6T_b$	73,54	16,32	4,44	69,40	100	52,57

Source: The author.

Figures 36a and 36b are gray scale plots of the temperature distribution surrounding the droplet with $T_\infty = 3T_b$ and $T_\infty = 6T_b$ case, respectively. The temperature distribution for $T_\infty = 3T_b$ case (Fig.36a) shows a highly strained flame with a thin plume in the outflow region. In contrast, the $T_\infty = 6T_b$ case (Fig. 36b) yield a thick plume and smoothly gradient of temperature around the droplet.

Figure 36 – Temperature field for (a) $T_\infty = 3T_b$ and (b) $T_\infty = 6T_b$.
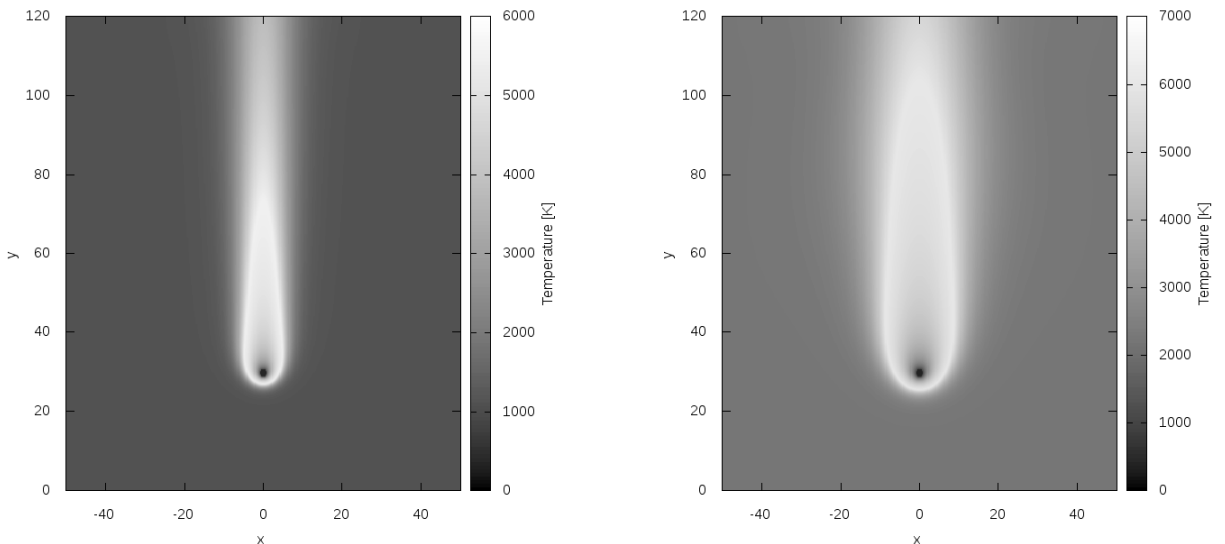
Source: The author.

5 CONCLUSIONS

The combustion of fuel being injected through a porous sphere was analyzed by numerical simulation under normal and microgravity conditions with different ambient temperatures. The effect of buoyancy was analyzed through the change of the gravity source term on momentum conservation equations. The source term depends on the difference between the density close to the droplet and the density far from the droplet ($\rho - \rho_\infty$). Thus the acceleration of the hot gases is induced by the gradient of the ambient temperature.

Initially, a verification of the code was made comparing the numerical predictions with the analytical solution in a zero gravity environment. The numerical result shows good agreement with the analytical, with a small over-prediction for the flame dimensions. The numerical zero gravity solution was compared with a normal gravity solution by its streamlines and temperature field. The results show the expected behavior for these two conditions, an elongated flame with asymmetrical flow for normal gravity, and a spherical flame with a symmetric flow for zero gravity condition.

The main objective of the present investigation was to analyze the ambient condition that can substantially change the flame shape. The results presented in this work show that when the ambient temperature increases, the velocity gradient and buoyancy source term decreases. Despite that, the flame standoff radius, height and width increase with the ambient temperature. The results have also shown that increasing the ambient temperature, the temperature gradient in the flame decreases affecting the flame position.

Appendix A – Analytical Solution

The mathematical model and assumptions described in Section 2.1 are used to depict analytically the combustion phenomenon of isolated pure fuel droplet under microgravity condition. The problem is described by the spherical uni-dimensional conservation equations of mass, energy and species:

$$\frac{1}{r^2}\frac{\partial}{\partial r}(r^2\rho u) = 0 \tag{A.1}$$

$$\frac{1}{r^2}\frac{\partial}{\partial r}\left(r^2\rho u\left\{\begin{array}{c} T \\ Y_O \\ Y_F \end{array}\right\}\right) = \frac{1}{r^2}\frac{\partial}{\partial r}\left(T^n r^2\frac{\partial}{\partial r}\left\{\begin{array}{c} T \\ Y_O \\ Y_F \end{array}\right\}\right) + \left\{\begin{array}{c} Q \\ -s \\ -1 \end{array}\right\}\dot{W} \tag{A.2}$$

Integrating A.1:

$$r^2\rho u = \dot{m} \tag{A.3}$$

where $\dot{m} = M/a_0^2\rho_b u_c$.

The Eqs. A.2 could be written as:

$$\frac{\dot{m}}{r^2}\frac{\partial}{\partial r}\left\{\begin{array}{c} T \\ Y_O \\ Y_F \end{array}\right\} = \frac{1}{r^2}\frac{\partial}{\partial r}\left(T^n r^2\frac{\partial}{\partial r}\left\{\begin{array}{c} T \\ Y_O \\ Y_F \end{array}\right\}\right) + \left\{\begin{array}{c} Q \\ -s \\ -1 \end{array}\right\}\dot{W} \tag{A.4}$$

Combining Eqs. A.4 in a way to appear $Z = sY_F - Y_O + 1$ and $H = (s+1)T/Q + Y_O + Y_F$ and for this, multiply the Eq.A.4.b with s and Eq.A.4.a with (-1) and summing

$$\frac{\dot{m}}{r^2}\frac{\partial}{\partial r}(sY_F - Y_O) = \frac{1}{r^2}\frac{\partial}{\partial r}\left[r^2\frac{\partial}{\partial r}(sY_F - Y_O)\right] = 0 \tag{A.5}$$

The reactive term disappears. Then,

$$\dot{m}\frac{\partial Z}{\partial r} = \frac{\partial}{\partial r}\left(r^2\frac{\partial Z}{\partial r}\right) \tag{A.6}$$

Performing the corresponding operations to obtain H, then

$$\dot{m}\frac{\partial H}{\partial r} = \frac{\partial}{\partial r}\left(r^2\frac{\partial H}{\partial r}\right) \tag{A.7}$$

The boundary conditions are

$$Z(1) = S+1, \qquad\qquad Z(\infty) = 0 \qquad\qquad \text{(A.8a)}$$

$$H(1) = \frac{(S+1)}{Q}T_b + 1, \qquad H(\infty) = \frac{(S+1)}{Q}T_\infty + 1 \qquad \text{(A.8b)}$$

Integrating Eqs.A.6 and A.7

$$C_1 + \dot{m}Z = r^2\frac{\partial Z}{\partial r} \quad\longrightarrow\quad \dot{m}(Z - \overline{C_1}) = r^2\frac{\partial Z}{\partial r} \qquad \text{(A.9)}$$

$$C_2 + \dot{m}H = r^2\frac{\partial H}{\partial r} \quad\longrightarrow\quad \dot{m}(H - \overline{C_2}) = r^2\frac{\partial H}{\partial r} \qquad \text{(A.10)}$$

Integrating Eqs.A.9 and A.10

$$\frac{\dot{m}}{r^2} = \frac{\partial Z}{\partial r}\frac{1}{(Z - \overline{C_1})} \quad\longrightarrow\quad \frac{\dot{m}}{r^2} = \frac{\partial}{\partial r}ln(Z - \overline{C_1})$$

$$-\dot{m}\frac{1}{r} = \frac{ln(Z - \overline{C_1})}{\widehat{C_1}}$$

$$Z - \overline{C_1} = \widehat{C_1}e^{\left(-\frac{\dot{m}}{r}\right)} \qquad \text{(A.11)}$$

$$H - \overline{C_2} = \widehat{C_2}e^{\left(-\frac{\dot{m}}{r}\right)} \qquad \text{(A.12)}$$

Applying the boundary conditions A.8a into the Eq A.11, then

$$Z(\infty) - \overline{C_1} = \widehat{C_1}e^{\left(-\frac{\dot{m}}{\infty}\right)}$$

$$\overline{C_1} = -\widehat{C_1} \qquad \text{(A.13)}$$

$$Z + \widehat{C_1} = \widehat{C_1}e^{\left(-\frac{(\dot{m})}{r}\right)} \qquad \text{(A.14)}$$

in $Z(1) = (S+1)$,

$$(S+1) + \widehat{C_1} = \widehat{C_1}e^{(-\dot{m})} \qquad \text{(A.15)}$$

$$(S+1) = \widehat{C_1}\left(e^{(-\dot{m})} - 1\right)$$

$$\widehat{C_1} = \frac{(S+1)}{e^{(-\dot{m})} - 1} \qquad \text{(A.16)}$$

Then

$$Z + \widehat{C_1} = \widehat{C_1}e^{\left(-\frac{(\dot{m})}{r}\right)} \tag{A.17}$$

$$Z = -\left(\frac{S+1}{e^{(-\dot{m})}-1}\right) + \left(\frac{S+1}{e^{(-\dot{m})}-1}\right)e^{\left(-\frac{(\dot{m})}{r}\right)}$$

$$\boxed{Z = \frac{S+1}{1-e^{(-\dot{m})}}\left(1-e^{\left(-\frac{(\dot{m})}{r}\right)}\right)} \tag{A.18}$$

Applying the boundary conditions A.8b into the Eq.A.12,

$$H(\infty) - \overline{C_2} = \widehat{C_2}e^{\left(-\frac{(\dot{m})}{\infty}\right)} \tag{A.19}$$

$$\widehat{C_2} = H(\infty) - \overline{C_2} \tag{A.20}$$

Then

$$H - \overline{C_2} = (H(\infty) - \overline{C_2})e^{\left(-\frac{(\dot{m})}{r}\right)} \tag{A.21}$$

For $r = 1$

$$H(1) - \overline{C_2} = (H(\infty) - \overline{C_2})e^{(-\dot{m})}$$

$$H(1) - H(\infty)e^{(-\dot{m})} = \overline{C_2}(1 - e^{(-\dot{m})})$$

$$\overline{C_2} = \frac{H(1) - H(\infty)e^{(-\dot{m})}}{1 - e^{(-\dot{m})}} \tag{A.22}$$

Then

$$\widehat{C_2} = H(\infty) - \frac{H(1) - H(\infty)e^{(-\dot{m})}}{1 - e^{(-\dot{m})}} \tag{A.23}$$

$$H = \widehat{C_2}e^{\left(-\frac{(\dot{m})}{r}\right)} + \overline{C_2}$$

$$H = \left(H(\infty) - \frac{H(1) - H(\infty)e^{(-\dot{m})}}{1 - e^{(-\dot{m})}}\right)e^{\left(-\frac{(\dot{m})}{r}\right)} + \frac{H(1) - H(\infty)e^{(-\dot{m})}}{1 - e^{(-\dot{m})}}$$

$$\boxed{H = H(\infty)e^{\left(-\frac{(\dot{m})}{r}\right)} + \left(\frac{H(1) - H(\infty)e^{(-\dot{m})}}{1 - e^{(-\dot{m})}}\right)(1 - e^{\left(-\frac{(\dot{m})}{r}\right)})} \tag{A.24}$$

The flame position is determined for $Z(rf) = 1$ in the Eq.A.18

$$1 = (S+1)\left(\frac{1-e^{\left(-\frac{(\dot{m})}{rf}\right)}}{1-e^{(-\dot{m})}}\right)$$

$$\frac{1-e^{(-\dot{m})}}{(S+1)} = 1-e^{\left(-\frac{(\dot{m})}{rf}\right)}$$

$$e^{\left(-\frac{(\dot{m})}{rf}\right)} = 1-\frac{1-e^{(-\dot{m})}}{(S+1)}$$

$$-\frac{(\dot{m})}{rf} = \ln\left[1-\frac{1-e^{(-\dot{m})}}{(S+1)}\right]$$

$$\frac{(\dot{m})}{rf} = \ln\left[1-\frac{1-e^{(-\dot{m})}}{(S+1)}\right]^{-1}$$

$$\boxed{rf = \frac{(\dot{m})}{\ln\left[1-\frac{1-e^{(-\dot{m})}}{(S+1)}\right]^{-1}}}$$

(A.25)

BIBLIOGRAPHY

ABRAMZON, B.; SIRIGNANO, W. Droplet vaporization model for spray combustion calculations. **International journal of heat and mass transfer**, Elsevier, v. 32, n. 9, p. 1605–1618, 1989.

ACKERMAN, M.; WILLIAMS, F. A. Simplified model for droplet combustion in a slow convective flow. **Combustion and flame**, Elsevier, v. 143, n. 4, p. 599–612, 2005.

ANNAMALAI, K.; PURI, I. K. **Combustion science and engineering**. [S.l.]: CRC press, 2006.

BEJAN, A.; KRAUS, A. D. **Heat transfer handbook**. [S.l.]: John Wiley & Sons, 2003. v. 1.

CHAUVEAU, C.; BIROUK, M.; GÖKALP, I. An analysis of the d 2-law departure during droplet evaporation in microgravity. **International Journal of Multiphase Flow**, Elsevier, v. 37, n. 3, p. 252–259, 2011.

CHIANG, C.; RAJU, M.; SIRIGNANO, W. Numerical analysis of convecting, vaporizing fuel droplet with variable properties. **International journal of heat and mass transfer**, Elsevier, v. 35, n. 5, p. 1307–1324, 1992.

CHOI, M. Y.; KYEONG-OKK, L. Investigation of sooting in microgravity droplet combustion. In: ELSEVIER. **Symposium (International) on Combustion**. [S.l.], 1996. v. 26, n. 1, p. 1243–1249.

CHORIN, A. J. A numerical method for solving incompressible viscous flow problems. **Journal of computational physics**, Elsevier, v. 2, n. 1, p. 12–26, 1967.

DIETRICH, D. L.; HAGGARD, J.; DRYER, F. L.; NAYAGAM, V.; SHAW, B. D.; WILLIAMS, F. A. Droplet combustion experiments in spacelab. In: ELSEVIER. **Symposium (International) on Combustion**. [S.l.], 1996. v. 26, n. 1, p. 1201–1207.

DIETRICH, D. L.; NAYAGAM, V.; HICKS, M. C.; FERKUL, P. V.; DRYER, F. L.; FAROUK, T.; SHAW, B. D.; SUH, H. K.; CHOI, M. Y.; LIU, Y. C. et al. Droplet combustion experiments aboard the international space station. **Microgravity Science and Technology**, Springer, v. 26, n. 2, p. 65–76, 2014.

DWYER, H. A.; SANDERS, B. R. A detailed study of burning fuel droplets. In: ELSEVIER. **Symposium (International) on Combustion**. [S.l.], 1988. v. 21, n. 1, p. 633–639.

EIGENBROD, C. European microgravity combustion science, from drop towers to the space station. **Annales Academia Scientiarium et Artium Europea**, 1999.

FACHINI, F. F. An analytical solution for the quasi-steady droplet combustion. **Combustion and flame**, Elsevier, v. 116, n. 1, p. 302–306, 1999.

FAETH, G. Evaporation and combustion of sprays. **Progress in Energy and Combustion Science**, Elsevier, v. 9, n. 1, p. 1–76, 1983.

FAROUK, T. I.; DRYER, F. L. On the extinction characteristics of alcohol droplet combustion under microgravity conditions–a numerical study. **Combustion and Flame**, Elsevier, v. 159, n. 10, p. 3208–3223, 2012.

FLETCHER, C. **Computational techniques for fluid dynamics 2: Specific techniques for different flow categories**. [S.l.]: Springer Science & Business Media, 2012.

GODSAVE, G. Studies of the combustion of drops in a fuel spray—the burning of single drops of fuel. In: ELSEVIER. **Symposium (International) on Combustion**. [S.l.], 1953. v. 4, n. 1, p. 818–830.

GOLDSMITH, M. On the burning of single drops of fuel in an oxidizing atmosphere. **Journal of Jet Propulsion**, v. 24, n. 4, p. 245–251, 1954.

GOLLAHALLI, S. R.; BRZUSTOWSKI, T. Experimental studies on the flame structure in the wake of a burning droplet. In: ELSEVIER. **Symposium (International) on Combustion**. [S.l.], 1973. v. 14, n. 1, p. 1333–1344.

HEYWOOD, J. **Internal combustion engine fundamentals**. [S.l.]: McGraw-Hill Education, 1988.

ISODA, H.; KUMAGAI, S. New aspects of droplet combustion. In: ELSEVIER. **Symposium (International) on Combustion**. [S.l.], 1958. v. 7, n. 1, p. 523–531.

JIANG, T. L.; CHEN, W. S.; TSAI, M. J.; CHIU, H. H. A numerical investigation of multiple flame configurations in convective droplet gasification. **Combustion and flame**, Elsevier, v. 103, n. 3, p. 221–238, 1995.

KASSOY, D. R.; WILLIAMS, F. A. Variable property effects on liquid droplet combustion. **AIAA Journal**, v. 6, n. 10, p. 1961–1965, 1968.

KING, M. K.; ROSS, H. D. Overview of the nasa microgravity combustion program. **AIAA journal**, v. 36, n. 8, p. 1337–1345, 1998.

KUO, K. K. Principles of combustion. John Wiley & Sons, Inc., 2005.

LAW, C. Recent advances in droplet vaporization and combustion. **Progress in energy and combustion science**, Elsevier, v. 8, n. 3, p. 171–201, 1982.

LAW, C.; FAETH, G. Opportunities and challenges of combustion in microgravity. **Progress in Energy and Combustion Science**, Elsevier, v. 20, n. 1, p. 65–113, 1994.

LAW, C. K. **Combustion physics**. [S.l.]: Cambridge university press, 2006.

MANZELLO, S. L.; CHOI, M. Y.; KAZAKOV, A.; DRYER, F. L.; DOBASHI, R.; HIRANO, T. The burning of large n-heptane droplets in microgravity. **Proceedings of the Combustion Institute**, Elsevier, v. 28, n. 1, p. 1079–1086, 2000.

MEGARIDIS, C. M.; SIRIGNANO, W. Numerical modeling of a vaporizing multicomponent droplet. In: ELSEVIER. **Symposium (International) on Combustion**. [S.l.], 1991. v. 23, n. 1, p. 1413–1421.

MITSUYA, M.; HANAI, H.; SAKURAI, S.; OGAMI, Y.; KOBAYASHI, H. Droplet combustion experiments in varying forced convection using microgravity environment. **International journal of heat and fluid flow**, Elsevier, v. 26, n. 6, p. 914–921, 2005.

OBERKAMPF, W. L.; TRUCANO, T. G. Verification and validation in computational fluid dynamics. **Progress in Aerospace Sciences**, Elsevier, v. 38, n. 3, p. 209–272, 2002.

PAN, K.-L.; LI, J.-W.; CHEN, C.-P.; WANG, C.-H. On droplet combustion of biodiesel fuel mixed with diesel/alkanes in microgravity condition. **Combustion and Flame**, Elsevier, v. 156, n. 10, p. 1926–1936, 2009.

POPE, D. N.; GOGOS, G. Numerical simulation of fuel droplet extinction due to forced convection. **Combustion and Flame**, Elsevier, v. 142, n. 1, p. 89–106, 2005.

PRAKASH, S.; SIRIGNANO, W. Theory of convective droplet vaporization with unsteady heat transfer in the circulating liquid phase. **International Journal of Heat and Mass Transfer**, Elsevier, v. 23, n. 3, p. 253–268, 1980.

PURI, I. K. **Environmental implications of combustion processes**. [S.l.]: CRC Press, 1993.

PURI, I. K.; LIBBY, P. A. The influence of transport properties on droplet burning. **Combustion science and technology**, Taylor & Francis, v. 76, n. 1-3, p. 67–80, 1991.

RAGHAVAN, V.; BABU, V.; SUNDARARAJAN, T.; NATARAJAN, R. Flame shapes and burning rates of spherical fuel particles in a mixed convective environment. **International journal of heat and mass transfer**, Elsevier, v. 48, n. 25, p. 5354–5370, 2005.

RENKSIZBULUT, M.; YUEN, M. Numerical study of droplet evaporation in a high-temperature stream. **Journal of Heat transfer**, American Society of Mechanical Engineers, v. 105, n. 2, p. 389–397, 1983.

SIRIGNANO, W. A. **Fluid dynamics and transport of droplets and sprays**. [S.l.]: Cambridge University Press, 1999.

SPALDING, D. B. The combustion of liquid fuels. In: ELSEVIER. **Symposium (international) on combustion**. [S.l.], 1953. v. 4, n. 1, p. 847–864.

SUH, H. K. Experiments and theoretical approaches on the burning behaviors of single n-heptane droplet. **Journal of Mechanical Science and Technology**, Springer, v. 29, n. 5, p. 2249–2257, 2015.

TURNS, S. R. An introduction to combustion. 2nd. **Boston: M cGraw Hill**, 2000.

ULZAMA, S.; SPECHT, E. An analytical study of droplet combustion under microgravity: Quasi-steady transient approach. **Proceedings of the combustion institute**, Elsevier, v. 31, n. 2, p. 2301–2308, 2007.

VUJANOVIĆ, M. **Numerical modelling of multiphase flow in combustion of liquid fuel**. 2010. Tese (Doutorado) — Fakultet strojarstva i brodogradnje, Sveučilište u Zagrebu, 2010.

WILLIAMS, A. Combustion of droplets of liquid fuels: a review. **Combustion and flame**, Elsevier, v. 21, n. 1, p. 1–31, 1973.

____. **Combustion of liquid fuel sprays**. [S.l.]: Butterworth-Heinemann, 1990.

WILLIAMS, F. A. Combustion theory, (1985). **Cummings Publ. Co**, 1985.

YOZGATLIGIL, A.; PARK, S.-h.; CHOI, M. Y.; KAZAKOV, A.; DRYER, F. L. Burning and sooting behavior of ethanol droplet combustion under microgravity conditions. **Combustion science and technology**, Taylor & Francis, v. 176, n. 11, p. 1985–1999, 2004.

YOZGATLIGIL, A.; PARK, S.-H.; CHOI, M. Y.; KAZAKOV, A.; DRYER, F. L. Influence of oxygen concentration on the sooting behavior of ethanol droplet flames in microgravity conditions. **Proceedings of the Combustion Institute**, Elsevier, v. 31, n. 2, p. 2165–2173, 2007.